JOURNAL OF AEROSPACE SOCIETY MALAYSIA

Volume 2, Issue 1

APRIL 2024

Papers from ISAE2023

Registration No. PPM-001-10-09012017

Toward Greater Heights

JOURNAL OF
AEROSPACE SOCIETY MALAYSIA

VOLUME 2, ISSUE 1
April 2024
Selected Papers from 3rd International Seminar on Aeronautics and Energy (ISAE) 2023

eISSN 3009-0520

B-31-09, Kompleks EVO, Jalan Pusat Bandar 2, Seksyen 9,
43650 Bandar Baru Bangi, Selangor, Malaysia

Email: aeros_journal@aerosmalaysia.my

Journal of Aerospace Society Malaysia (AEROS Journal) is an open-access online journal that publishes high-quality research articles in all areas of aeronautics, astronautics and aviation. All submitted articles will undergo peer-review process before they are accepted for publication.

Publication Frequency: 3 times a year (end of April, August and December)

EDITORIAL

EDITOR-IN-CHIEF

LIST OF REVIEWERS FOR THIS ISSUE

PREFACE

International Seminar on Aeronautics and Energy (ISAE)
25th October 2023
Universiti Teknologi Malaysia, Kuala Lumpur, Malaysia

Universiti Teknologi Malaysia Aeronautical Laboratory (UTM Aerolab) is a specialized research laboratory and a center of excellence in Universiti Teknologi Malaysia. The laboratory is set-up mainly to meet the educational and research needs of Malaysia's developing aerospace industry. The goals are to provide education and training of undergraduate engineers in a variety of aerospace fields, provide facility to foster postgraduate and industrial research in aerospace and related fields, and also to offer aerodynamic testing services to industry.

UTM Aerolab, in conjunction with UTM NEXUS Expo 2023, organized International Seminar on Aeronautics and Energy 2023 (ISAE 2023). The purpose of the conference is to bring educators, researchers, engineers and industry players working in the area of aeronautics, energy and related fields together. Aeronautical and energy industry are the growing component for ASEAN and world nowadays. Therefore, ISAE 2023 is a platform to bring all the key players together. The conference received many paper submissions, which were all presented orally during the conference. Several selected papers from the ISAE 2023 are published in this issue of Journal of Aerospace Society Malaysia.

UTM Aerolab wishes to thank everyone who contributed to the success of this special issue, especially both authors and reviewers, as well as the AEROS Journal editorial team, for their invaluable support and assistance.

ASSOC. PROF. IR. DR. SHABUDIN BIN MAT
CHAIRMAN OF ISAE 2023 CONFERENCE,
UNIVERSITI TEKNOLOGI MALAYSIA,
KUALA LUMPUR, MALAYSIA.

TABLE OF CONTENTS

JOURNAL OF AEROSPACE SOCIETY MALAYSIA

ARTICLE

EFFECT OF AEROFOIL THICKNESS ON THE WIND TURBINE BLADE: CASE STUDY OF FFA-W3-270 AND FFA-W3-240 AEROFOIL

Nur Natasha Ayuni Nazri [1,*] and Shabudin Mat [1]

1. UTM Aerolab, Institute for Vehicle System & Engineering (IVeSE), Universiti Teknologi Malaysia, Malaysia.

*Correspondence: nurnatashaayuni@gmail.com

Abstract: Due to the climate change nowadays, there are a lot of alternative ways to convert renewable energy to generate electricity and the wind energy is one of them. Reynold's numbers of 0.8×10^6 and 1.0×10^6 are compared in this study to see their effects on the FFA-W3-270 and FFA-W3-240 aerofoil models. The dimension of the FFA-W3-240 type is 120 mm thick, with a chord of 500 mm and a span of 800 mm. In contrast, the FFA-W3-270 type has 128 mm maximum thickness, 500 mm chord and a span of 750 mm. Investigation of the lift force, drag force, pitching moment and pressure distributions on these two aerofoil models is done in a wind tunnel test using UTM LST Wind Tunnel, which has dimensions of 1.5 m x 2 m x 5.8 m. The wind tunnel experiments are carried out at 25 m/s and 31.2 m/s wind stream velocity and angle of attack ranging from -4 ° to 18 ° with an increment of 2°. From the experimental results, it is observed that the pressure coefficient on the upper surface of the FFA-W3-240 has a significant change in comparison to that for the FFA-W3-270. When the adverse pressure gradient increases, it causes earlier separation for thinner aerofoil. In contrast, it causes separation delay for the thick aerofoil. From this, it shows that FFA-W3-270 has better aerodynamic performance. For FFA-W3-240, at Reynold's number 1.0×10^6, stall occurs at 14° with maximum lift coefficient of 1.26. However, for FFA-W3-270, stall does not occur up until 18°. Besides, for FFA-W3-240, increasing the Reynold's number will increase the drag coefficient at stall point by over 5.48%. For both models, the pitching moment coefficient remains relatively constant over the considered range of angles of attack due the moment being calculated at the aerodynamic center of the aerofoil, which is estimated to be at the quarter-chord location from the leading edge.

Keywords: aerofoil; separation; angle of attack; aerodynamic performance; stall

1. Introduction

Utilizing wind energy typically has a lower environmental impact than using other energy sources. Most buildings now use small-sized wind turbines, especially industrial buildings. The function of this wind turbine is to convert kinetic energy from the rotation of the turbine that is caused by the passing wind into mechanical energy and subsequently, it will be converted into electrical energy. Wind turbines can be divided into two primary categories: horizontal-axis turbines (HAWT) and vertical-axis turbines (VAWT) [1]-[2]. In general, the aerodynamic issues faced by wind turbine operations are mostly caused by adverse pressure gradient, which causes flow separation. The capacity to lessen, regulate or postpone the flow separation will significantly improve an airfoil's aerodynamic performance and consequently will help boost the efficiency of a general turbine [3]. In a recent study, several methods to improve the performance of horizontal wind turbine blades are investigated, which is focused on utilizing multiple airfoil sections and fence [4]. Based on the findings, it has been suggested that these enhancements can lead to improved efficiency and performance of horizontal wind turbines.

For the presented study in this paper, a specialized FFA aerofoil model is used. Among others, this aerofoil design has been developed for the purpose of overcoming the weakness of high drag and low maximum lift coefficient, C_{Lmax} that many thick airfoils commonly exhibit with rough leading [5]. In the previous studies, conducted numerical analysis on the effect of changing thickness to the aerodynamic performance of the aerofoil has demonstrated that increasing the aerofoil thickness will lead to increase in drag coefficient and maximum lift [6]-[7]. Moreover, an analysis on the aerodynamic characteristics of the FFA-W3-270 aerofoil has found that the maximum suction peak value at the leading edge on the suction side varies dramatically when the angle of attack increases, even though the value on the bottom surface does not [8]. This means that, when the Reynolds number rises, the maximum lift will increase, the drag coefficient will decrease and the stall condition will occur at lower angle of attack.

While previous studies have shown that the thickness of the aerofoil has significantly affected the wing's aerodynamic properties, it should be noted that most of these earlier studies used the simulation analysis methods, with only very few involved the experimental trials. Because of this, there is a lack of experimental data for comparison purposes. More specifically, the data for the FFA aerofoil is not well-documented. This study is addressing this identified gap of information.

2. Methodology

In this research, two types of FFA-W3 aerofoil are tested: FFA-W3-240 and FFA-W3-270. These two aerofoil are shown in Figure 1 while the experimental setup for the wind tunnel testing are tabulated in Table 1. Both aerofoil models are tested in the wind tunnel for varied angles of attack between -4° and 18° with 2° increment under two settings of Reynolds' number: 0.8×10^6 and also 1.0×10^6. The LabVIEW application software is used for data acquisition utilizing the computer data logger.

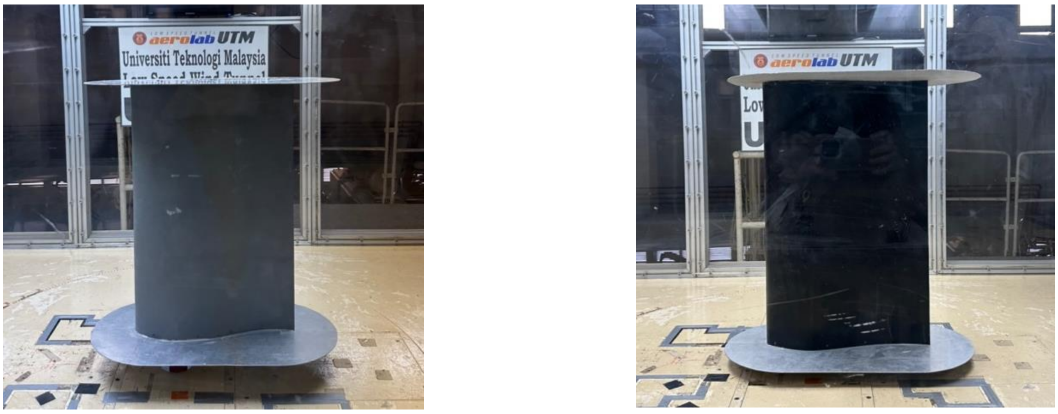

(a) FFA-W3-270 aerofoil

(b) FFA-W3-240 aerofoil

Figure 1: Test models used in this study

Table 1: Experimental setup for the wind tunnel testing

Aerofoil Model	Pressure Taps	Model Size
FFA-W3-270	30 (17 on the upper surface and 13 on the lower surface)	Total span: 750 mm Chord: 500 mm Maximum thickness: 135 mm
FFA-W3-240	36 (21 on the upper surface and 15 on the lower surface)	Total span: 800 mm Chord: 500 mm Maximum thickness: 120 mm

From the experiments, the main results that will be measured are the surface pressure distribution, aerodynamic forces and moments. The FKPS 30DP electronic pressure scanner is used to monitor the surface pressure and an external balance is used to measure the aerodynamic forces and moments. The technical drawing for the FFA-W3-270 model and the illustration on how the model is set up inside the wind tunnel are shown in Figure 2 and Figure 3, respectively.

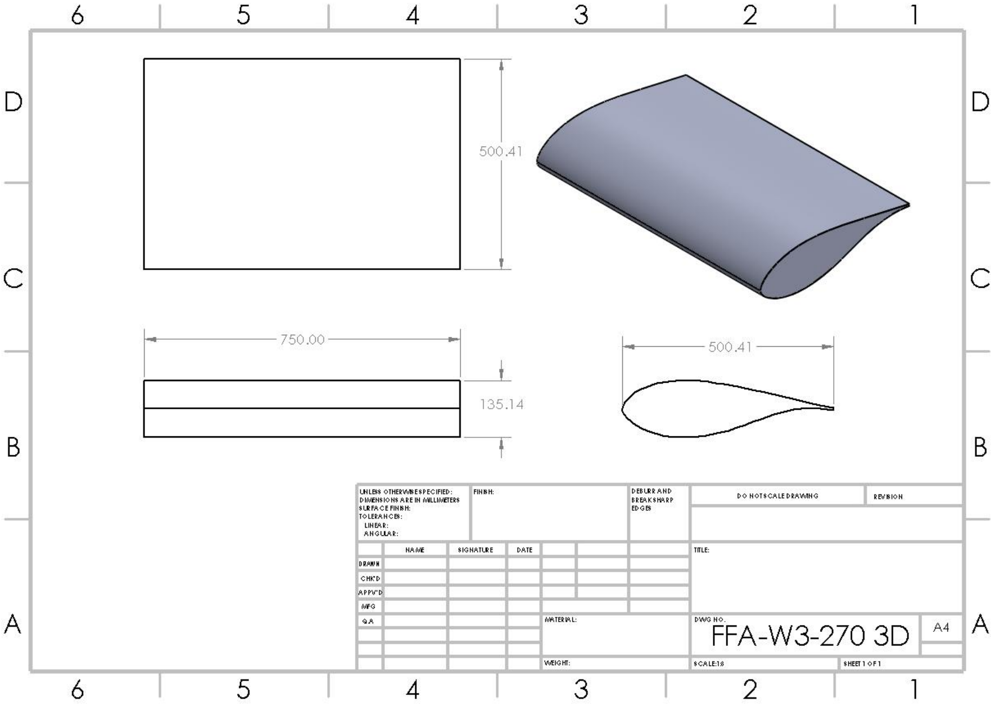

Figure 2: Technical drawing of FFA-W3-270 aerofoil

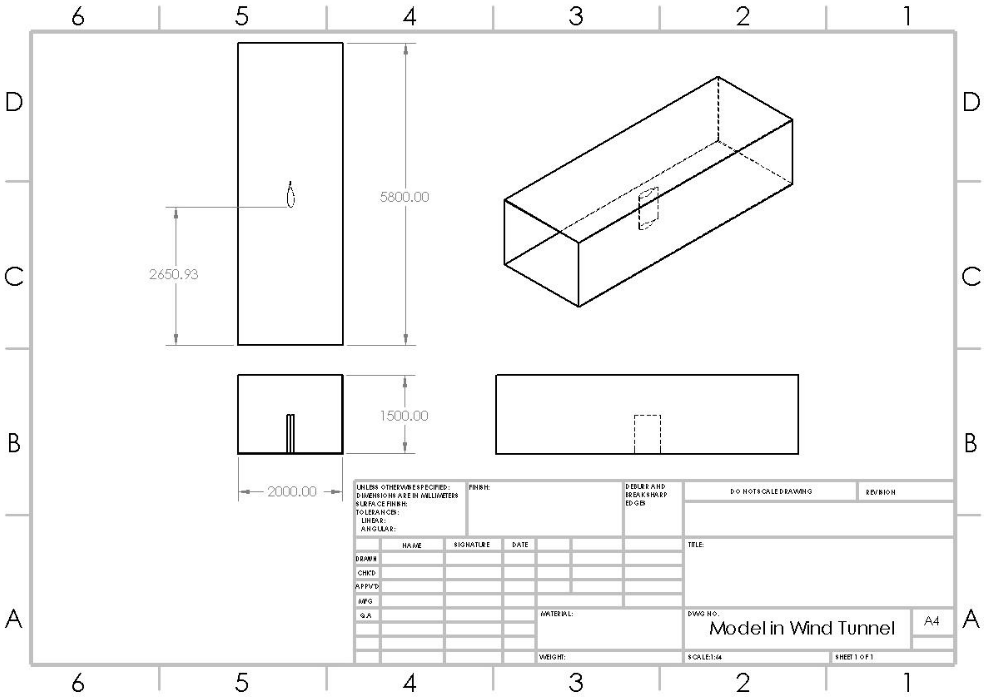

Figure 3: Orientation of the test model in wind tunnel during testing

Figure 4 shows the overall flowchart for the data collection. The data are collected from the wind tunnel testing include lift coefficient (C_L), drag coefficient (C_D), pitching moment coefficient (C_M) and surface pressure of location (X/C) of the aerofoil's pressure coefficient (C_P).

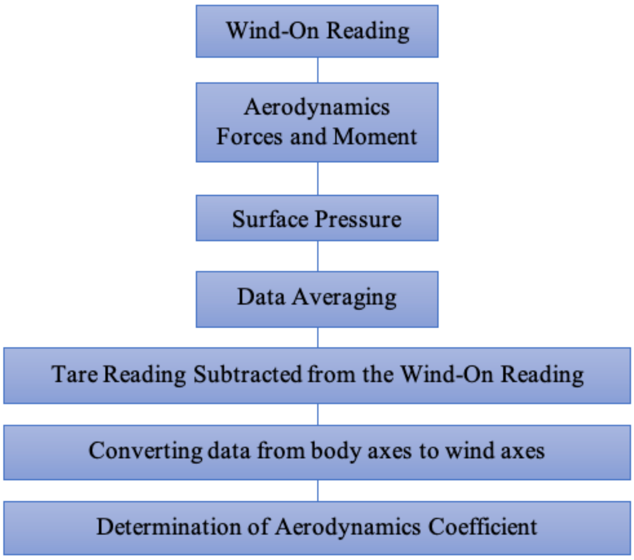

Figure 4: Overall flowchart of data collection and analysis process in this study

3. Results and Discussion

As depicted in Figure 5, for both aerofoil models at angle of attack of -4°, the pressure coefficient, C_P of the lower surface is lower than that of the upper surface at the leading edge. Moving down to the trailing edge, at $X/C = 0.612$, the C_P value for both upper and lower surfaces intersects, after which C_P for the lower surface increases gradually. This shows that the pressure for lower surface at the leading edge is lower than the freestream pressure. Furthermore, as shown in Figure 6 for both aerofoil models, at angle of attack of 0°, C_P value for the upper surface is lower than that for the lower surface. With further increase in angle of attack, for example as indicated by Figure 7 for angle of attack of 10°, the maximum suction peak value at the leading edge on the suction side significantly changes whereas the value for the lower surface does not change much. It can be observed that C_P on the upper surface of the FFA-W3-240 aerofoil has a big significant change compared to that for the FFA-W3-270 aerofoil.

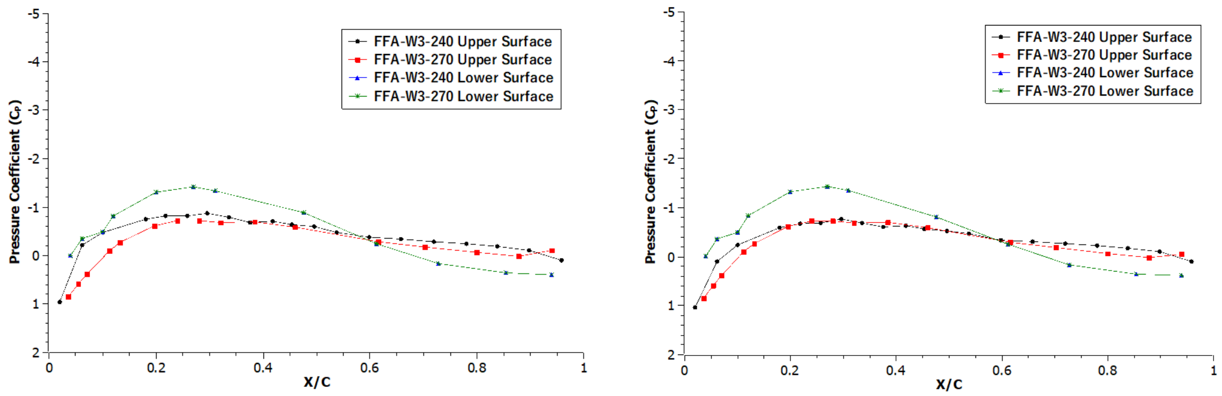

(a) Re = 0.8 × 10^6 (b) Re = 1.0 × 10^6

Figure 5: *Cp* versus X/C at angle of attack of -4°

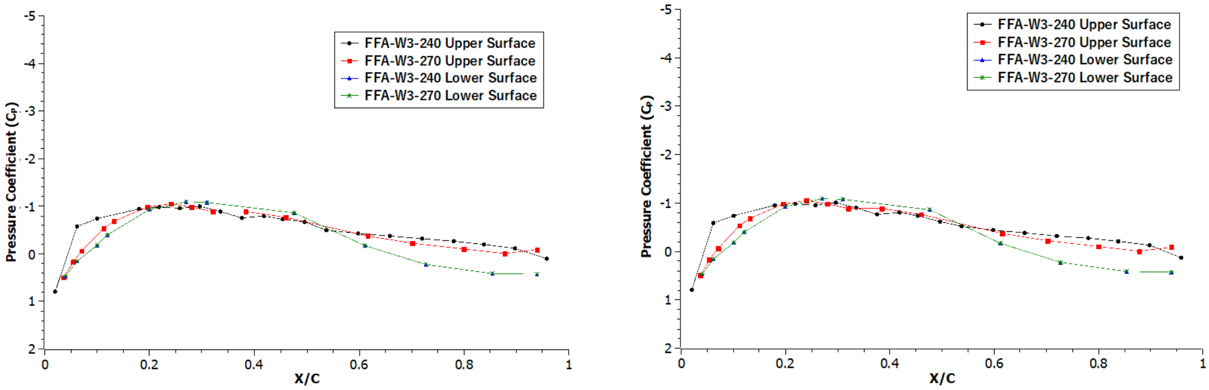

(a) Re = 0.8 × 10^6 (b) Re = 1.0 × 10^6

Figure 6: Cp versus X/C at angle of attack of 0°

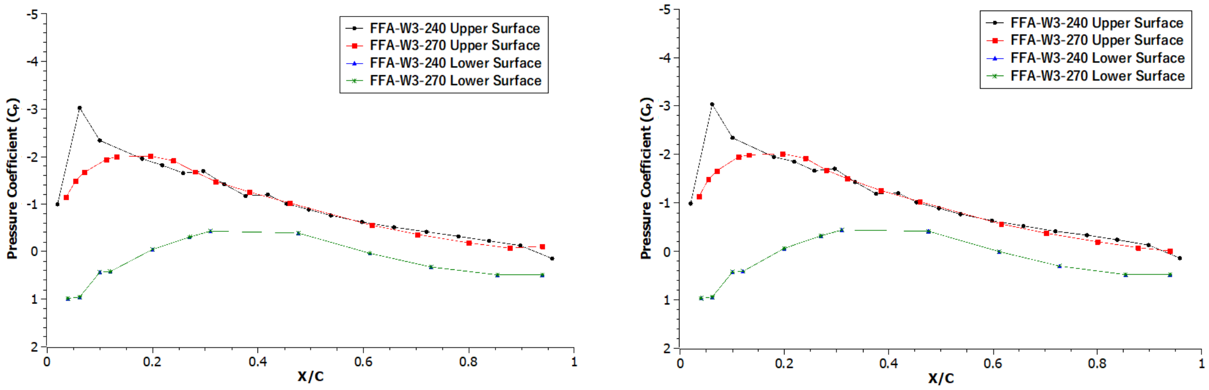

(a) Re = 0.8 × 10^6 (b) Re = 1.0 × 10^6

Figure 7: Cp versus X/C at angle of attack of 10°

The full separation starts to occur after the stall angle. By comparing the plot for angle of attack of 16° in Figure 8 and angle of attack of 18° in Figure 9, the separation point can be seen to start moving forward. For instance, this situation can be observed for the upper surface of the FFA-W3-270 aerofoil in Figure 8 and Figure 9 whereby as the angle of attack increases, the maximum C_P value starts to move towards leading edge. This observation is in line with findings from other studies that, as the angle of attack increases, the separation points progressively shift towards the leading edge [9]-[10].

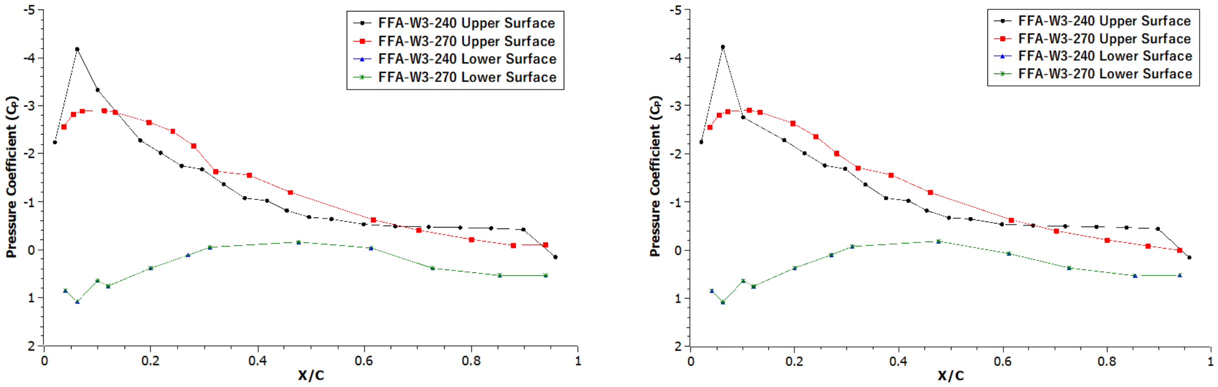

(a) Re = 0.8 × 10^6 (b) Re = 1.0 × 10^6

Figure 8: Cp versus X/C at angle of attack of 16°

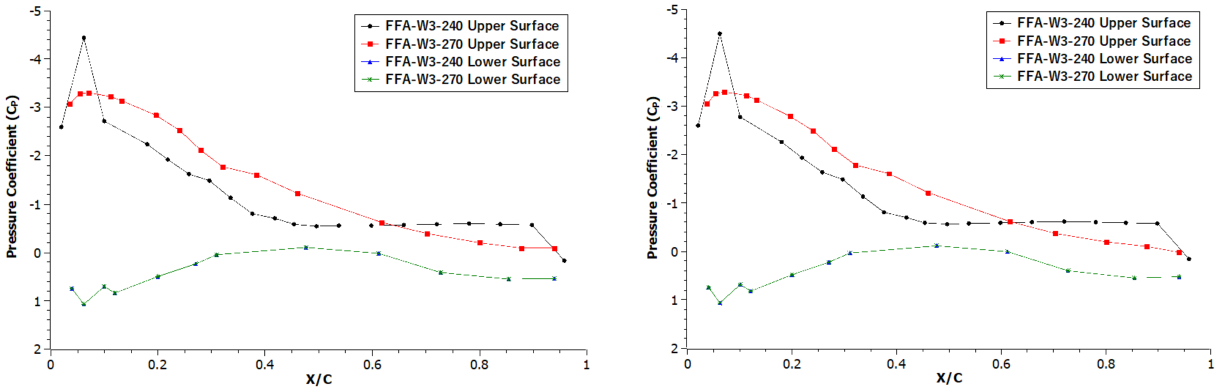

(a) Re = 0.8×10^6 (b) Re = 1.0×10^6

Figure 9: Cp versus X/C at angle of attack of 18°

Moreover, as indicated by Figure 7, the adverse pressure gradient begins to appear at angle of attack of 10°. When the adverse pressure gradient increases, it will cause earlier separation for thinner aerofoil but separation delay for thick aerofoil. Relative thickness affects the aerofoil performance by changing the location and size of the laminar separation bubble. In the meantime, it can be seen that increasing Reynold's number is not much affecting the pressure distribution of both aerofoil except at low angles.

Meanwhile, as shown in Figure 10 for Reynolds number of 1.0×10^6, stall occurs at angle of attack of 14° with maximum lift coefficient 1.26 for FFA-W3-240 aerofoil. On contrary, stall does not occur up until angle of attack of 18° for the FFA-W3-270 aerofoil with the same Reynolds number of 1.0×10^6 as depicted in Figure 11. Overall, both plots follow the typical trend of C_L versus angle of attack. Once the angle of attack exceeds the stalling angle, the separation occurs and the lift reduces [11]-[12]. As depicted in Figure 10, increasing the Reynold's number also increases the maximum lift coefficient for the FFA-W3-240 model. However, effect of Reynold's number is negligible for the FFA-W3-270 aerofoil as can be observed in Figure 11.

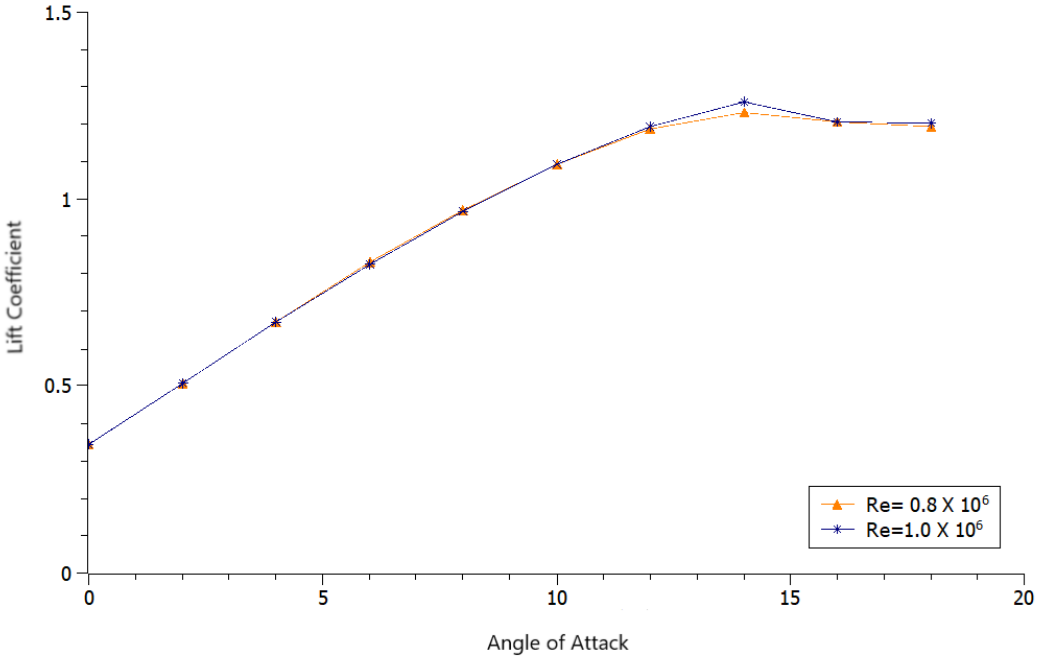

Figure 10: C_L versus angle of attack for FFA-W3-240 aerofoil

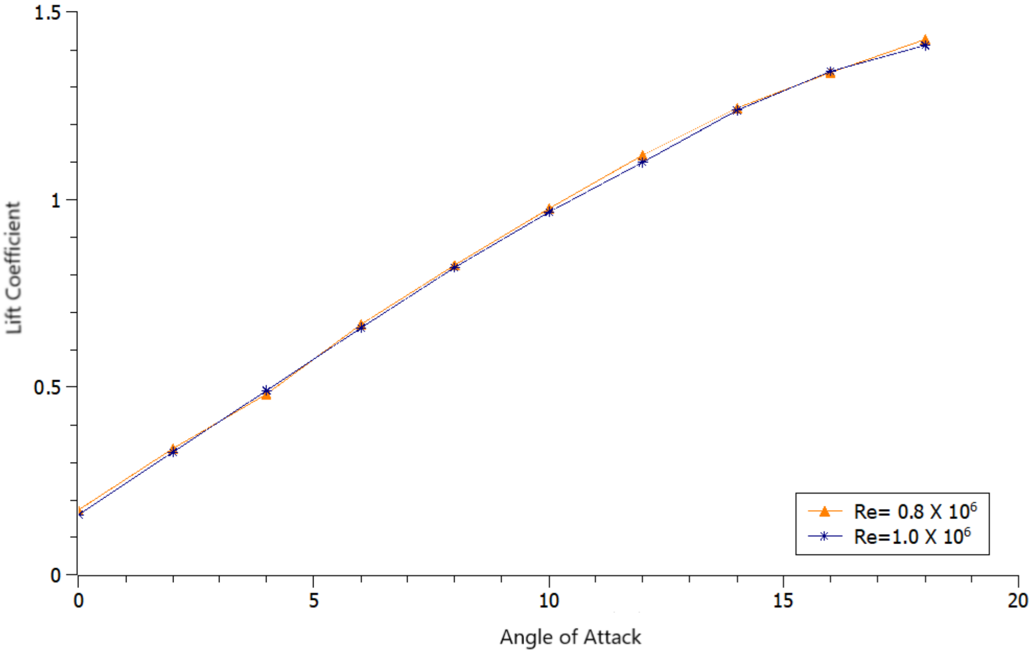

Figure 11: C_L versus angle of attack for FFA-W3-270 aerofoil

On the other hand, Figure 12 and Figure 13 depict the plot of C_D versus angle of attack for FFA-W3-240 and FFA-W3-270 aerofoil, respectively. For FFA-W3-240 aerofoil, at Reynolds number of 1.0 × 10^6, the drag coefficient at stall angle is shown to increase by over 5.48% compared to that at Reynolds number of 0.8 × 10^6. However, variation of Reynolds number has insignificant effect on drag coefficient value for the FFA-W3-270 aerofoil. The findings are in line with the results in another study, which has discovered that increasing the thickness of the aerofoil is associated with higher drag coefficient and an earlier occurrence of flow separation on the upper surface of the aerofoil [6].

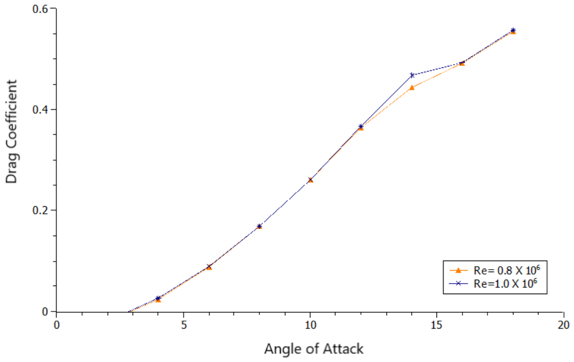

Figure 12: C_D versus angle of attack for FFA-W3-240 aerofoil

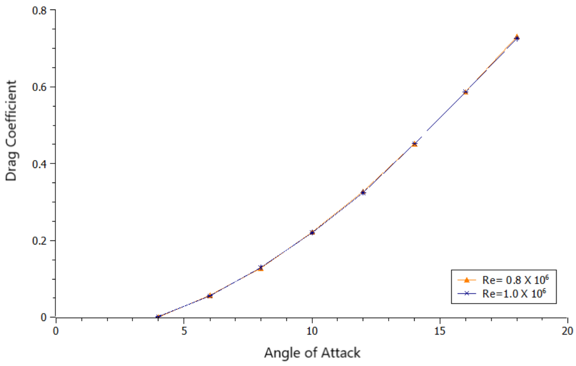

Figure 13: C_D versus angle of attack for FFA-W3-270 aerofoil

Last but not least, the resultant pitching moment coefficient of both FFA-W3-240 and FFA-W3-270 aerofoil are shown in Figure 14 and Figure 15, respectively. For FFA-W3-240 aerofoil, at Reynolds number of 1.0 × 10^6, the value of pitching moment coefficient at stall point is slightly higher than that at Reynolds number of 0.8 × 10^6. After the stall angle, the pitching moment coefficient start to decrease. This situation can be contributed to the flow separation during stall that leads to significant decrease in lift generation. Since the pitching moment coefficient is a measure of the balance between the lift forces acting on airfoil, the reduced lift after stall contributes to a decrease in the pitching moment coefficient.

Both FFA-W3-240 and FFA-W3-270 aerofoil are engineered to maintain a relatively constant pitching moment coefficient across a spectrum of angles of attack. Furthermore, since the moment coefficient is computed around the aerodynamic center point ($C/4$), influence of angle of attack is minimized [8].

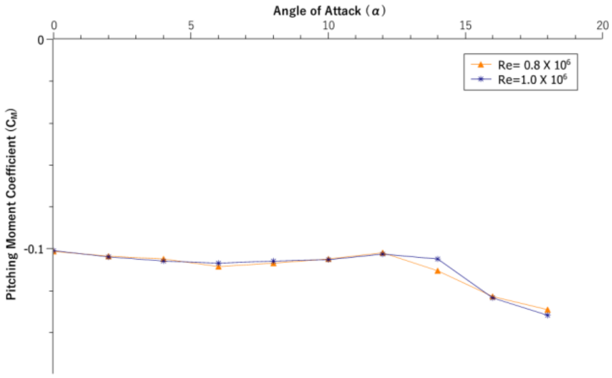

Figure 14: C_M versus angle of attack for FFA-W3-240 aerofoil

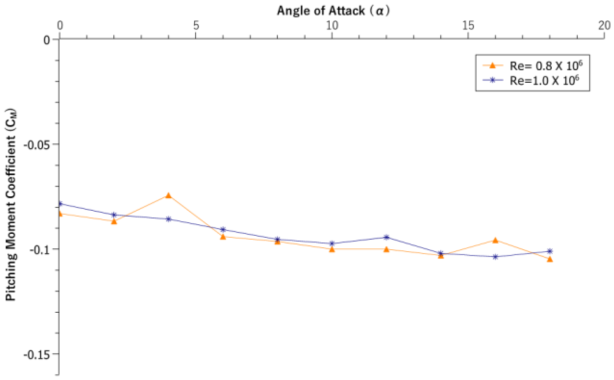

Figure 15: C_M versus angle of attack for FFA-W3-270 aerofoil

4. Conclusion

When compared to FFA-W3-270 aerofoil, it is found that pressure coefficient on the upper surface of FFA-W3-240 aerofoil has undergone a significant change. When the adverse pressure gradient grows, it causes separation to occur sooner for thinner airfoils but later for thicker airfoils. The findings from this study demonstrate that FFA-W3-270 aerofoil performs better than FFA-W3-240 aerofoil because a high performance requires the flow attachment to be maintained for as long as possible to maximize the lift generation. Regarding the lift coefficient, a higher maximum relative thickness results in a greater maximum lift. Elevating the Reynolds number boosts the maximum lift coefficient for FFA-W3-240 at Reynolds number of 1.0×10^6 with lift coefficient of 1.26 at angle of 14°. On contrary, for FFA-W3-270, stall does not occur until 18°. Increasing the Reynolds number for FFA-W3-240 amplifies the drag coefficient at the stall point by over 5.48%. For both aerofoil, the pitching moment coefficient remains relatively constant across various angles of attack. In the future works, it is advised to change the angle of attack up to 30° and alter the Reynolds number to notice more on the flow separation especially on the FFA-W3-270 aerofoil.

Acknowledgement

The authors would like to thank Aerolab UTM (Universiti Teknologi Malaysia) for the use of their facilities and everybody involved who shared their expertise and assistance. Their guidance and financial support are much appreciated.

References

[1] M. Scungio, F. Arpino, V. Focanti, M. Profili and M. Rotondi, ‘Wind Tunnel Testing of Scaled Models of Newly Developed Darrieus-style Vertical Axis Wind Turbine with Auxiliary Straight Blades’, Energy Conversion and Management, vol. 130, pp. 60-70, 2016.

[2] O. F. Marzuki, A. S. Mohd Rafie, F. I. Romli and K. A. Ahmad, ‘Magnus Wind Turbine: The Effect of Sandpaper Surface Roughness on Cylinder Blades’, Acta Mechanica, vol. 229, pp. 71-85, 2018.

[3] L. Xu, L. Xu, L. Zhang and K. Yang, 'Design of Wind Turbine Blade with Thick Airfoils and Flatback and Its Aerodynamic Characteristic', The Open Mechanical Engineering Journal, vol. 9, no. 1, pp. 910-915, 2015.

[4] A. H. Muheisen, M. A. R. Yass, I. K. Irthiea, 'Enhancement of Horizontal Wind Turbine Blade Performance using Multiple Airfoils Sections and Fences', Journal of King Saud University - Engineering Sciences, vol. 35, no. 1, pp. 69-81, 2023.

[5] A. Bjorck, 'Coordinates and Calculation for the FFA-W1-xxx, FFA-W2-xxx and FFA-W3-xxx Series of Airfoils for Horizontal Axis Wind Turbines', Report No. FFA TN 1990-15, Aeronautical Research Institute of Sweden, 1990.

[6] O. A. Abdulkareem, A. F. Khudheyer and A. S. Abbas, 'Numerical Investigation of the Effect of Changing the Thickness of Airfoils Used in Wind Turbines on the Lift to Drag Ratio', IOP Conference Series: Materials Science and Engineering, vol. 1094, no. 1, 012078, 2021.

[7] D. Ma, Y. Zhao, Y. Qiao and G. Li, 'Effects of Relative Thickness on Aerodynamic Characteristics of Airfoil at a Low Reynolds Number', Chinese Journal of Aeronautics, vol. 28, no. 4, pp. 1003–1015, 2015.

[8] S. Jafari-Gahraz, T. B. Mat Lazim, G. E. Schneider and M. Darbandi, 'Experimental Study on Aerodynamic Performance of FFA-W3-270 Airfoil for Axial Wind Turbine Blade', Presented at International Conference of Fluid Flow, Heat and Mass Transfer, Ottawa, Canada, 2016.

[9] A. V. Arena and T. J. Mueller, 'Laminar Separation, Transition and Turbulent Reattachment Near the Leading Edge of Airfoils', AIAA Journal, vol. 18, no. 7, pp. 747-753, 1980.

[10] T. Nakano, N. Fujisawa, Y. Oguma, Y. Takagi and S. Lee, 'Experimental Study on Flow and Noise Characteristics of NACA0018 Airfoil', Journal of Wind Engineering and Industrial Aerodynamics, vol. 95, no. 7, pp. 511-531, 2007.

[11] F. I. Romli, M. A. Mohammad Sabri and R. E. Mohd Nasir, 'Optimization of a Blended-Wing-Body Unmanned Aerial Vehicle Design for Maximum Aerodynamic Lift-to-Drag Ratio', CFD Letters, vol. 15, no. 3, pp. 12-21, 2023.

[12] M. Z. Abdul Manaf, S. Mat, S. Mansor, T. Mat Lazim, W. K. Wan Ali, W. Z. Wan Omar, Z. Mohd Ali, A. Abdullatif and M. Abd Wahid, 'Influences of External Store on Aerodynamic Performance of UTM-LST Generic Light Aircraft Model', Journal of Advanced Research in Fluid Mechanics and Thermal Sciences, vol. 39, no. 1, pp. 36-46, 2017.

CONCEPTUAL DEVELOPMENT OF A PULVERIZED COAL COMBUSTOR RIG (PCCR) FOR TESTING CO-FIRING PULVERIZED COAL AND AMMONIA FUEL

Mohd Khairul Hafiz Md Lias [1,*], **Mazlan Abdul Wahid** [1] **and Norazila Othman** [2]

1. High Speed Reacting Flow Laboratory (HiREF), Department of Thermofluids, Faculty of Mechanical Engineering, Universiti Teknologi Malaysia, 81310 UTM Skudai, Johor, Malaysia.
2. Department of Aeronautics, Automotive and Ocean Engineering, Faculty of Mechanical Engineering, Universiti Teknologi Malaysia, 81310 UTM Skudai, Johor Malaysia

*Correspondence: mohdkhairulhafiz@graduate.utm.my

Abstract: In Malaysia, the National Energy Policy 2022 - 2040 is focusing on achieving global net-zero greenhouse gas (GHG) emissions by 2050. To accelerate the energy transition plan, the National Energy Transition Roadmap (NETR) has been developed, which also includes the development of hydrogen, H_2 and ammonia, NH_3 co-firing for power generation. The ammonia co-firing with coal has a significant effect on reducing carbon dioxide, CO_2 emissions but it also increases the nitrogen oxide, NOx content due to the high nitrogen content in its molecules. Additionally, the flame characteristic of the ammonia combustion has a narrow flammable range and slow flame propagation. Therefore, by introducing the ammonia injection swirl nozzle in the co-firing combustion, it enables a higher flammable range and increase flame propagation to achieve a higher temperature at the burner tip. The objective of this study is to conceptually develop a new test rig for co-firing pulverized coal and ammonia fuel with ammonia injection axial swirl nozzle. The significance of this development is to further improve GHG reduction for CO_2 and NO_X emissions. The conceptual test rig is designed for conducting experiments with the variation of axial swirl nozzle angle between 30^0 to 60^0 and also swirl number, S_n between 0.50 to 1.48. The test rig design concept is also expected to be able to test up to 100% ammonia firing.

Keywords: green fuel; pulverized coal; ammonia; co-firing; swirl nozzle

1. Introduction

In Malaysia, the National Energy Policy 2022 - 2040 has been implemented to achieve a global net-zero greenhouse gas (GHG) emissions by year 2050. To accelerate the energy transition, the Malaysian government has also developed the National Energy Transition Roadmap (NETR), which includes the development of hydrogen (H_2) and ammonia (NH_3) co-firing for power generation [1]-[2]. The interest in co-fired ammonia has been increasing to reduce GHG emission, particularly in carbon dioxide (CO_2) due to its carbon-free fuel [3]. The ammonia co-firing with coal has a significant effect on reducing CO_2 emissions [4]-[5]. Although H_2 and NH_3 have been known as alternative fuel for the carbon-free fuel, it also increases the nitrogen oxide, NOx content due to the high nitrogen content in their molecules. The combustion characteristic of H_2 and NH_3 will enable the NOx formation, fuel-NOx, thermal-NOx and prompt-NOx at specific conditions during combustion. Furthermore, the flame characteristic of ammonia combustion has a narrow flammable range and a slow flame propagation [3]-[4]. Nonetheless, the NOx formation from NH_3 and H_2 combustion can be possibly controlled with proper combustor and new technology. One of the proposed ways for this is by introducing the ammonia injection swirl nozzle in the co-firing combustion, which will enable a higher flammable range and also increase flame propagation to achieve higher temperature at the burner tip. Based on the previous conducted studies, when the co-firing ratio increases between 20% and 30%, the flame will be changed from swirl flame to elongated flame [6]-[7].

In a previous experiment, the swirl vane angle is adjusted to reduce the flame length and obtain a similar result to that of the single coal combustion [7]. The flame appearance from this previous study is shown in Figure 1. However, experimental method to investigate the effect of flame characteristics and NOx emission when selecting different vane angles for the swirl nozzle has not yet been performed.

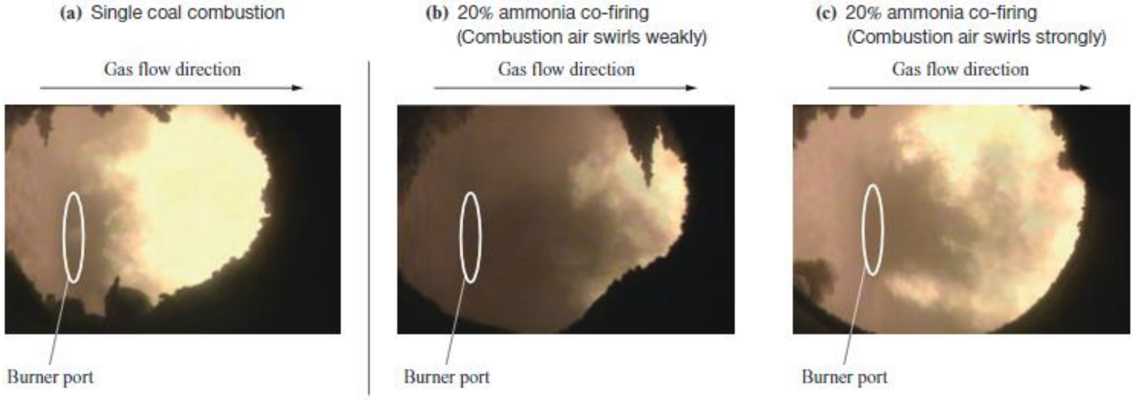
(a) Single coal combustion

(b) 20% ammonia co-firing (Combustion air swirls weakly)

(c) 20% ammonia co-firing (Combustion air swirls strongly)

Figure 1: Flame appearance: (a) single coal combustion; (b) 20% ammonia co-firing (combustion air swirls weakly; (c) 20% ammonia co-firing (combustion air swirls strongly) [7]

In the meantime, based on another previous experiment, the CO_2 emission is found to be reduced by increasing the co-firing ratio of ammonia [4], which is observed in Figure 2. By applying an ammonia axial swirl nozzle at different vane angles, it is expected to achieve higher reduction of CO_2. Moreover, by combining the air-staging method at several points and applying an ammonia axial swirl nozzle at a higher swirl number, $Sn \geq 0.60$, it is expected to achieve lower velocity at the burner exit and fuel-rich conditions occur at the burner zone and reduce NOx formation [8]-[9].

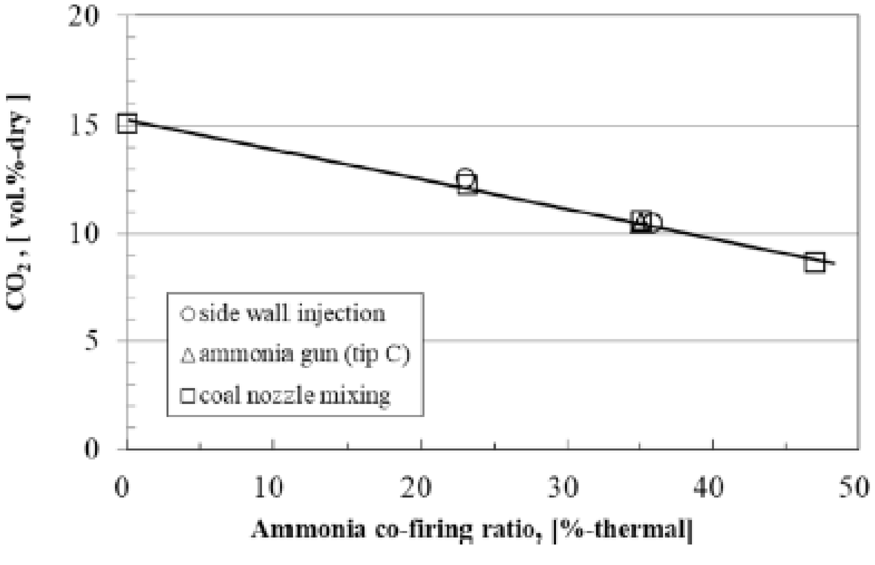

Figure 2: Change of CO_2 concentration due to ammonia co-firing ratio [4]

It should be noted that the flame characteristic has been separated into two main categories. The first is the flame length, type, size and color, which are measured by using high-speed camera and quartz combustion chamber. Second is to determine the flame temperature and combustion emission, which is in CO_2 and NO_X emission. The flame characteristic when co-firing with 20% ammonia is to be away from the burner port compared with single coal combustion [7]. This is because the flame propagation velocity of ammonia co-firing with pulverized coal is higher than firing with pure coal. Figure 3 shows the comparison of flame appearance that is more stable when ammonia co-fired with other combustion fuel such as methane.

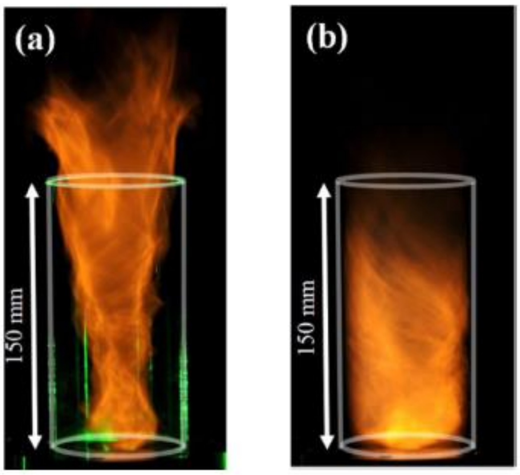

Figure 3: (a) Pure liquid ammonia spray flame; (b) Liquid ammonia spray flame co-fired with methane [10]

In conjunction to the abovementioned findings, the objective of this study is to develop a new test rig design for co-firing pulverized coal and ammonia fuel using an ammonia injection axial swirl nozzle. The test rig is designed and developed to be used to conduct experiments with variable axial swirl nozzle angle between 30^0 to 60^0 and the swirl number, S_n between 0.50 to 1.48. By having this test rig, the right setting could be tested to lower CO_2 emissions. It is expected that CO_2 emission significantly decreases concurrently with increase of the co-firing ratio while NOx emission can be further reduced at higher swirl number, $S_n \geq 0.60$.

2. Methodology

In this study, the test rig is conceptually designed and developed to analyze the flame characteristic and combustion emission of CO_2 and NO_X gases when co-firing ammonia and pulverized coal. Based on the findings in the literatures and established requirements for the intended experiments that will be conducted using the test rig, design concept for the test rig can be derived. Among others, the developed test rig will be comprised of burner, furnace, ammonia injection gun, pulverized coal bin, and primary and secondary air supply. The pulverized coal burner consists of an ammonia gun at the center of the coal nozzle for ammonia gas injection, secondary air with the swirl air vane and an annular coal nozzle to supply pulverized coal with primary air. A summary of the overall methodology for this study, starting from the selection of fuel and up to the analysis of the flame characteristics and pollutant (CO_2 and NO_X) emissions in co-firing pulverized coal and ammonia, is depicted in Figure 4. However, it should be noted that the presented study in this paper only covers the conceptual design development of the test rig. The expected experiments from the use of this test rig requires the capability to vary several of the parameters such as ammonia injection axial swirl nozzle vane angle, ammonia mass flow rate, co-firing ratio for ammonia and also secondary air vane angle.

The design for test rig, known as Pulverized Coal Combustor Rig (PCCR), consists of fuel system supply and furnace body for combustion and pollutant emission monitoring system. Each section in the PCCR is developed according to the intended experiments that will be conducted using it, which include to determine the flame characteristics, temperature of the flame and pollutant (CO_2 and NO_X) emissions concentration during testing with single fuel using pulverized coal and co-firing pulverized coal with ammonia injection.

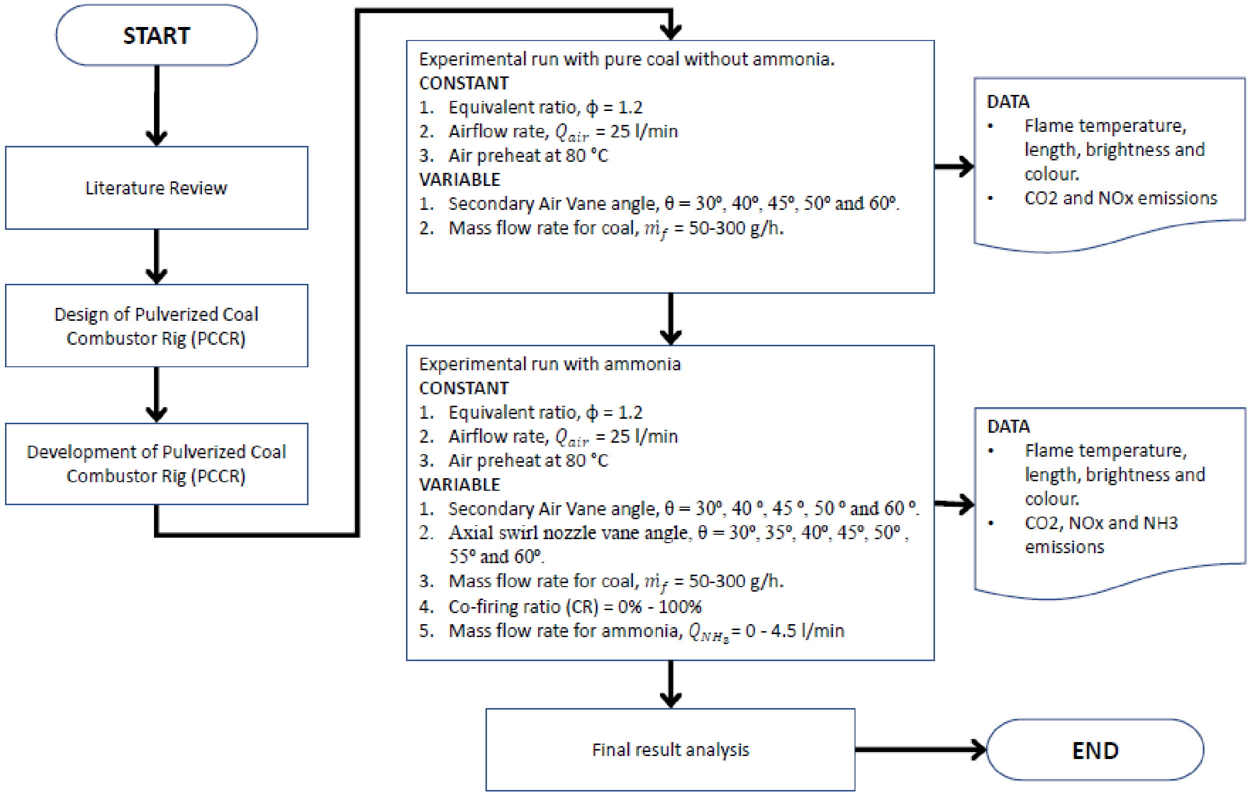

Figure 4: Flowchart of the combustion analysis of co-firing pulverized coal and ammonia from the use of the proposed test rig design

Based on the flowchart in Figure 4, an initial test will be conducted once the test rig has been fully developed. The initial testing is without ammonia to acquire the stable flame from the single fuel using pulverized coal. In this initial testing, the value for equivalent ratio, Φ is kept constant at 1.2 by adjusting the mass flow rate for pulverized coal and airflow rate from the air compressor. The air supply is heated to 80 °C through an electric heater before premixed with the pulverized coal. Both secondary air vane angle and also mass flow rate for coal are adjusted to optimize the swirl effect and obtain a stable flame. The flame characteristic is recorded for its brightness, length, color and temperature. The gas analyzer measures the CO_2 and NO_X gas concentration at the furnace exhaust in part per million (ppm) unit.

Once satisfied with the results of the initial test, the following experiment to be conducted using the test rig will use ammonia as secondary fuel for co-firing with the pulverized coal. Mass flow rate for ammonia fuel, mass flow rate for coal and airflow rate are adjusted to maintain the constant value of the equivalent ratio, Φ at 1.2. The air supply from air compressor is heated to 80 °C to supply hot air for premixed pulverized coal before entering the burner nozzle. The ammonia fuel is injected into the burner from the center of the tip nozzle. The co-firing ratio is assessed by increasing the mass flow rate of ammonia and reducing the mass flow rate for pulverized coal, which is tested up to 100% firing with ammonia. The ammonia nozzle has an axial swirl angle to produce high turbulence recirculation zone, which will stabilize the flame. The experiment with co-firing ammonia is using different nozzles with specific angle (i.e. θ = 30°, 35°, 40°, 45°, 50°, 55° and 60°). In the similar fashion to the initial test, the flame characteristics will be recorded and CO_2, NO_X and NH_3 gas concentration at the furnace exhaust will be measured by the gas analyzer.

Figure 5 illustrates the features of the experimental setup for the PCCR, including one-dimensional test furnace body, coal feeder, burner, staged air-providing system, flue gas sampling and monitoring system, and flue gas processing system. The test furnace body is a cylindrical quartz chamber with an internal diameter of 80 mm and a total length of 1000 mm, where the pulverized coal residence time can reach between 3.5 s to 4.2 s. The experimental rig is installed with a burner nozzle equipped with an ammonia injection gun tip at the center and an ammonia flow meter to control the flow rate and the co-firing ratio between ammonia and coal percentage.

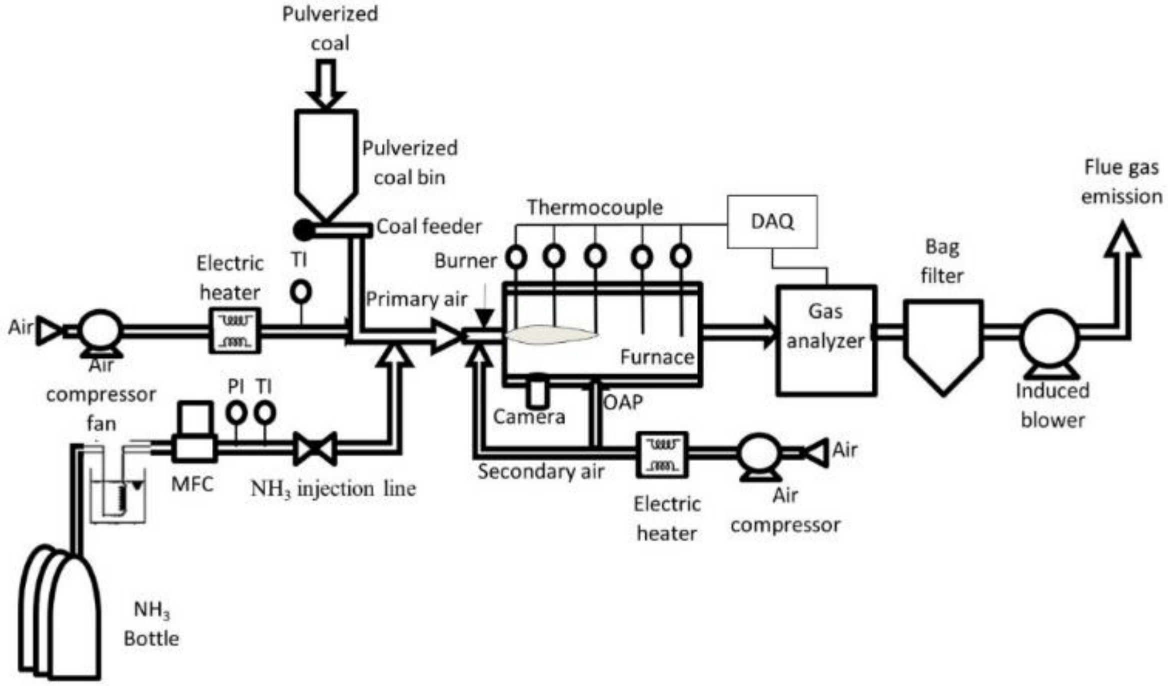

Figure 5: Schematic drawing of the Pulverized Coal Combustion Rig (PCCR)

The flame characteristic is monitored and recorded visually for its length, shape and color using a high-definition camera as shown in Figure 6(a). Secondary air vane angle for the swirler, θ that provides the secondary air into the furnace is adjusted from 30° to 60°. For this experiment, seven different vane angles for ammonia injection axial swirl nozzle are analyzed, which are 30°, 35°, 40°, 45°, 50°, 55° and 60°. Furthermore, gas properties for NO_X, CO_2 and NH_3 are analyzed in real-time monitoring by using gas analyzer, DURAG Emission Monitoring system. The flame temperature is measured at the installed thermocouple (TC) inside the furnace body at different distance from the burner tip (TC1, TC2, TC3, TC4 and TC5). The interval between the thermocouple is 50 mm from the burner throat and 200 mm between each thermocouple. The flame temperature is then recorded in the Data Acquisition (DAQ) system every 5 s during the experiment as shown in Figure 6(b).

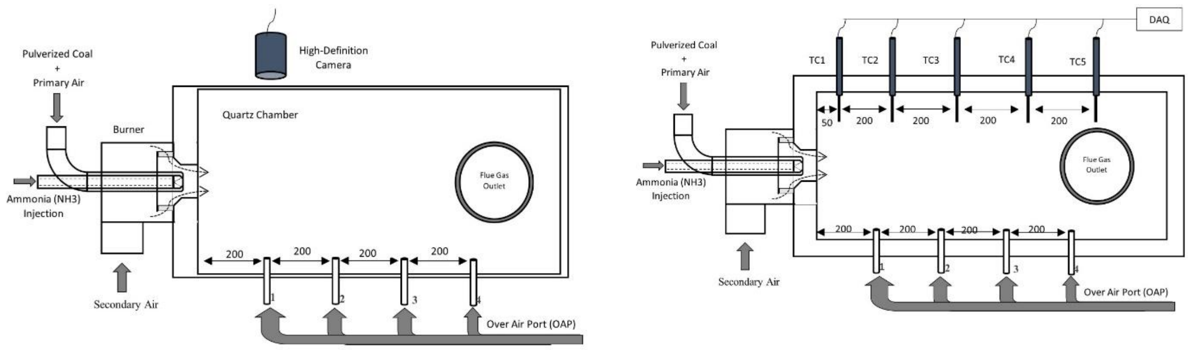

(a) Burner and quartz chamber with high-definition camera

(b) Burner and quartz chamber with thermocouple

Figure 6: Furnace (a) to capture flame shape; (b) to measure flame temperature.

During the conduct of the experiment, the co-firing of ammonia and coal is performed to measure the effect of co-firing on both flame characteristics and combustion emission. It should be noted that the method used in this study is similar to other experiments using a bench-scale 1.2 MW-thermal coal-fired furnace to determine the effect of combustion emission on CO_2 and NOx using ammonia as co-firing fuel [4]. The pulverized coal is fed by the screw feeder with special ejector and the feeding rate of 50 g/h to 300 g/h. Moreover, the experiment involves adjustment of co-firing ratio with variable mass flow rate for coal between 50 g/h and 300 g/h, and mass flow rate for ammonia between zero and 4.5 l/min. The axial swirl nozzle angle is adjusted at seven different angles from 30^{o} to 60^{o} and the swirl number, S_n is tested between 0.50 and 1.48. Swirling induces a high turbulence recirculation zone, which stabilizes the flame, resulting in better mixing and combustion. In general, swirl is important to provide flame stability since it creates central reverse-flow zone [9, 11]. It also provides stable combustion and rapid heat release.

On the other hand, the pulverized coal burner consists of swirl air vanes, an annular type of coal nozzle and an ammonia injection gun that is located in the center of the burner. A single burner, which consists of a coal nozzle and ammonia injection gun, is mounted on one end. An indirect firing system is used and the pulverized coal is fed into the pulverized coal bin and transported using compressed air from the air compressor. The airflow rate, Q_{air} is 25 l/min and the excess air ratio (equivalent ratio) is fixed at 1.2. The compressed air is preheated using the electric heater to supply the high temperature of the air at 80 °C into the burner [12]-[13]. About 15% to 30% of the theoretical air, which is called the primary air, is supplied by the compressed air [14]. In this experiment, the coal mass flow rate is constant between 0 g/min to 3 g/min.

Last but not least, the safety of ammonia handling also needs to be taken care of according to the Chemical Safety Data Sheet (CSDS). Ammonia is classified as flammable, toxic and hazardous to human and aquatic life. Appropriate Protective Personal Equipment (PPE) including splash-proof goggles, neoprene rubber glove, face shield, respirator with ammonia filter cartridge, high boots, long sleeve shirt and long pants and boots for chemical handling. The most important area to be protected is the area exposed to the eye and skin because ammonia can cause severe skin burns and eye damage.

3. Results and Discussion

Based on the established design requirements, the PCCR test rig is developed to specifically capture the flame characteristics and monitor the combustion emissions when co-firing pulverized coal with ammonia. The design concept for the test rig is divided into three main sections. The first section is the fuel supply where the pulverized coal will be fed through the coal feeder and the ammonia liquid will be vaporized by hot water heater. The pulverized coal will be heated using supplied hot air where the heat source is an electric heater. In the meantime, the second section is the furnace body that is built in with high temperature resistance quartz chamber. This is where the burner nozzle that is equipped with an ammonia injection gun tip at the center is installed. The ammonia injection uses the axial swirl nozzle as the main variable to measure the stability of the flame during co-firing pulverized coal and ammonia. High-definition camera will be used to capture the flame characteristics whereas the flame temperature will be measured by the thermocouple. It can be noted that approximately five thermocouples will be installed at different distances from the burner tip. Finally, the third section is gas emission monitoring system using a gas analyzer to monitor the flue gas properties of CO_2 and NO_X during the experiment. The filter bag is installed to capture the fly ash exit from the furnace body to avoid from its release into the atmosphere. The gas analyzer will also monitor ammonia gas properties to ensure that the ammonia gas is within allowable limit. If the ammonia gas concentration exceeds the allowable limit, emergency shut down is taken immediately.

Swirling induces a high turbulence recirculation zone, which stabilizes the flame, resulting in better mixing and combustion. Swirl is important to provide flame stability because it creates central reverse-flow zone [9, 11]. It also provides stable combustion and rapid heat release. In terms of flame stability, the analysis using swirl burner nozzle tips for ammonia injection is crucial. It is expected to achieve a stable flame when using a swirl nozzle at swirl number, $S_n \geq 0.6$ [9]-[10]. Hence, the flame characteristic, flame temperature, and CO_2 and NO_X emission are analyzed using different burner swirl number, S_n as per Equation 1 and Table 1.

$$S_n = \frac{2}{3}\left[\frac{1-\left({D_i}/{D_o}\right)^3}{1-\left({D_i}/{D_o}\right)^2}\right]\tan\theta \tag{1}$$

Table 1: Ammonia injection axial swirl nozzle angle and swirl number [11]

Swirler No.	Vane angle for swirler, θ	Swirl number, S_n
1	30°	0.50
2	35°	0.60
3	40°	0.72
4	45°	0.86
5	50°	1.02
6	55°	1.22
7	60°	1.48

No. of vane: 10
Vane thickness, T_v: 0.5 mm
Hub diameter, D_i : 4.5 mm
Tip diameter, D_o : 6.5 mm
Swirl direction: counter clockwise

4. Conclusion

In this paper, the concept design of the test rig for conducting experiments of pulverized coal and ammonia co-firing has been developed. This new PCCR can be used to determine flame characteristic and also the effects of ammonia on combustion emissions of CO_2 and NO_X gases. The main sections for the test rig concept design can be divided into three major sections: (1) fuel supply, (2) furnace body for combustion, (3) gas emission monitoring. Once the test rig is developed and operational, it will be initially tested by conducting an experiment without ammonia fuel injection to obtain flame stability and expected CO_2 and NO_X emissions when firing with single fuel of pulverized coal. After achieving the required flame characteristics, and CO_2 and NO_X emission, the test rig will then be used to conduct experiment with co-firing of ammonia using injection axial swirl nozzle burner at different swirl angles. The co-firing ratio is determined by adjusting the mass flow rate for ammonia. In this experiment, the new PCCR test rig is expected to be capable to be tested up to 100% ammonia fuel and the gas analyzer can measure the excess of the ammonia gas. All in all, the new PCCR design concept is developed and has been discussed to be sufficient to measure flame characteristics and gas emission for CO_2 and NO_X. Following this conceptual development, the immediate future work involves the complete development of this test rig and it will be tested as outlined in the flowchart of the overall methodology.

Acknowledgement

This work is supported by Universiti Teknologi Malaysia (UTM), Combustion laboratory for all of the facilities provided, Tanjung Bin Power Plant for the sample of pulverized coal and it is also funded by a research group member for MOHE FRGS grant recipient under the Vote No. 5F595.

References

[1] Malaysian Ministry of Economy. (2023). National Energy Transition Roadmap. Retrieved from www.ekonomi.gov.my/sites/default/files/2023-09/National%20Energy%20Transition%20Roadmap _0.pdf
[2] International Energy Agency. (2022). World Energy Outlook 2022. Retrieved from www.iea.org /reports/world-energy-outlook-2022
[3] H. Kobayashi, A. Hayakawa, K. D. K. Somarathne and E. C. Okafor, 'Science and Technology of Ammonia Combustion', Proceedings of the Combustion Institute, vol. 37, no. 1, pp. 109-133, 2019.
[4] M. Tamura, T. Gotou, H. Ishii and D. Riechelmann, 'Experimental Investigation of Ammonia Combustion in a Bench Scale 1.2 MW-thermal Pulverised Coal Firing Furnace', Applied Energy, vol. 277, 115580, 2020.
[5] M. K. H. Md Lias and M. Abdul Wahid, 'Advance Thermal Configuration using Computational Fluid Dynamic in Co-Firing Coal and Biomass', AIP Conference Proceeding, vol. 2749, 060003, 2023.
[6] M. Liu, S. Chen, H. Zhu, Z. Zhou and J. Xu, 'Numerical Investigation of Ammonia/Coal Co-Combustion in a Low NOx Swirl Burner', Energy, vol. 282, 2023.
[7] H. Ishii, E. Ohno, T. Kozaki, T. Ito and T. Fujimoro, 'Developing of Co-Firing Technology of Pulverized Coal and Ammonia for Supressing NOx Generation', IHI Engineering Review, vol. 55, no. 2, 2022.
[8] T. Ito, H. Ishii, J. Zhang, S. Ishihara and T. Suda, 'New Technology of the Ammonia Co-Firing with Pulverized Coal to Reduce the NOx Emission', Presented at AIChE Annual Meeting, Orlando, USA, 2019.
[9] M. N. Rahman, N. Shahril, S. Yusup and I. Shariff, 'Hydrogen Co-Firing Characteristics in a Single Swirl Burner: A Numerical Analysis', IOP Conference Series: Materials Science and Engineering, vol. 1257, no. 1, 012020, 2022.
[10] E. C. Okafor, H. Yamashita, A. Hayakawa, K. K. A. Somarathne, T. Kudo, T. Tsujimura, M. Uchida, S. Ito and H. Kobayashi, 'Flame Stability and Emissions Characteristics of Liquid Ammonia Spray Co-Fired with Methane in a Single Stage Swirl Combustor', Fuel, vol. 287, 119433, 2021.

[11] S. Sheykhbaglou and S. M. Robati, ‘Effects of Coaxial Airflow Swirl Number on Combustion and Flame Characteristics of Methane/Air and n-Butane/Air Flames in a Miniature-Scale Swirl Burner’, Engineering Research Express, vol. 4, no. 2, 025045, 2022.

[12] M. Tamura, S. Watanabe, K. Komaba and K. Okazaki, ‘Combustion Behaviour of Pulverised Coal in High Temperature Air Condition for Utility Boilers’, Applied Thermal Engineering, vol. 75, pp. 445-450, 2015.

[13] X. Wang, W. Fan, J. Chen, G. Feng and X. Zhang, ‘Experimental Study and Kinetic Analysis of the Impact of Ammonia Co-Firing Ratio on Products Formation Characteristics in Ammonia/Coal Co-Firing Process’, Fuel, vol. 329, 125496, 2022.

[14] Z. Ouyang, W. Liu, C. Man, J. Zhu and J. Liu, ‘Experimental Study on Combustion, Flame and NO_X Emission of Pulverized Coal Preheated by a Preheating Burner’, Fuel Processing Technology, vol. 179, pp. 197-202, 2018.

JOURNAL OF AEROSPACE SOCIETY MALAYSIA

EXPERIMENTAL FLUTTER ANALYSIS WITH BENDING-TORSION COUPLING

Nurul Zubaidah Zaki [1], Haris Ahmad Israr Ahmad [1,*] and Muhammad Faruq Foong [1]

1. Aeronautics Laboratory, Faculty of Mechanical Engineering, Universiti Teknologi Malaysia, 81310 UTM Skudai, Johor, Malaysia.

*Correspondence: harisahmad@utm.my

Abstract: In short, bending-torsion coupling is a phenomenon that occurs when bending and torsional deformations of a structure are coupled. This can happen due to the geometry of the structure or due to the aerodynamic forces acting on the structure. Bending-torsion coupling can have significant impact on the flutter onset conditions of a structure. This study aims to presents the results of an experimental analysis of flutter for composite wing with bending-torsion coupling. The experiment is conducted in the low-speed wind tunnel (UTM-LST), where the carbon fiber composite wing with fiber orientation of $[30°]_4$ and $[45°]_4$ are placed on the test rig to mimic real flight condition. An accelerometer sensor is used in the experiment to measure the wing model's structure vibration in x-, y- and z-axis. The results of the experiment have shown that the composite wing with fiber orientation of $[30°]_4$ has higher flutter speed, which can be contributed to the existence of bending-torsion coupling due to its fiber laminate orientation.

Keywords: flutter; aeroelasticity; bending-torsion coupling; composite wing; fiber orientation

1. Introduction

Flutter is arguably the most important of all aeroelastic phenomena and it is also the most difficult to predict. In short, flutter can be described as an unstable self-excited vibration in which the structure extracts energy from the air stream and it can potentially lead to a catastrophic structural failure [1]-[3]. Nowadays, advanced composites are widely used in the aircraft and wing structures due to their material properties [4]. It has been estimated that about 30% of the aircraft structures are made of various types of advanced composites [5]. Due to its directional properties, the composite structures could be tailored accordingly to alter the structural deformation and avoid flutter [6]. In this case, the tailoring is done by changing the fiber orientations to exploit its advantages such as high strength to weight ratio, effective stiffness and high resistance to dynamic instability [7]. Furthermore, the influence of bending-torsion coupling should also be included in the analysis of composite wing, unlike that for metallic structures where such coupling does not exist due to their isotropic nature [8]. In a previously conducted analysis on the effects of bending-torsion coupling towards divergence, it has been found that stiffness coupling could be employed to delay the onset of stall flutter [9]. Additionally, according to another conducted study, the composite tailoring involving bending-torsion coupling seems to be effective for high aspect ratio and low aspect ratio wings [10]. Since flutter results from the interaction between inertial, elastic and aerodynamic forces, the aeroelastic equation of motion is applied in the flutter speed computation [11]. In order to have a better prediction of flutter speed, a suitable aerodynamic theory must be chosen. Some researchers have used v-g method, k method and p-k method in flutter analysis [9, 11].

The purpose of this study is to determine the effects of bending-torsion coupling stiffness towards the flutter speed. Classical laminate theory (CLT) is used in this study to conduct a parametric study on laminate orientation and stacking sequence by considering the bending-torsion coupling rigidities. The flutter speed is computed using the aeroelastic equation of motion by applying aerodynamic derivatives model and structural natural frequencies obtained from the finite element analysis. The data is validated by conducting experiment tests on the fabricated wing model with chosen laminate configurations. The experiment is conducted in the UTM low-speed wind tunnel.

2. Methodology

In this study, all three composite flat wing models used for the analysis are straight rectangular flat plates with different fiber orientations. All these composite wing models are fabricated using the same material of carbon fiber, which is Tenax-J HTS40 E13 3K 200tex by Composites Technology Research Malaysia (CTRM). The materials and geometry for all composite wings are respectively listed and shown in Table 1 and Figure 1.

Table 1: Material properties of Tenax-J HTS40 E13 3K

Parameters	Value
Young Modulus 0°, E_1	130 GPa
Young Modulus 90°, E_2	130 GPa
In-plane shear modulus, G_{12}	4 GPa
Poisson's ratio, ν_{12}	0.06
Density, ρ	1770 $\mathrm{kgm^{-3}}$
Thickness of one ply	0.0003 m
Grammage	200 $\mathrm{gm^{-2}}$

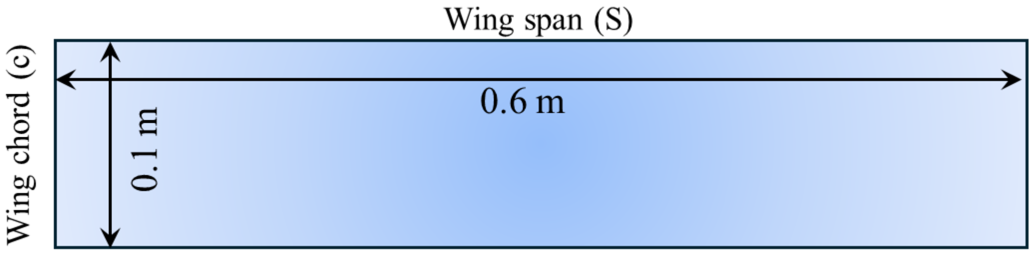

Figure 1: Composite flat wing geometry in this study

The selection of fiber orientation for the composite flat wing is conducted through a computational method with parameters obtained from [D] matrices derived from Classical laminate theory (CLT) as shown in Equation 1. From the theory, the bending-torsion coupling parameter can be obtained from the element D_{16}. Table 2 presents the bending stiffness matrix of each fiber orientation configuration varies from 0° to 45°. Moreover, calculation of bending-torsion coupling ratio is given by Equation 2.

$$\{M_x\ M_y\ M_{xy}\} = [D_{11}\ D_{12}\ D_{16}\ D_{12}\ D_{22}\ D_{26}\ D_{16}\ D_{26}\ D_{66}]\{k_x\ k_y\ k_{xy}\} \tag{1}$$

$$\text{Bending-torsion coupling ratio} = D_{16} \,/\, \sqrt{\frac{D_{11}}{D_{66}}} \tag{2}$$

Variation of the bending-torsion stiffness coupling ratio against the fiber orientation is illustrated in Figure 2. From Figure 2, it is found that the highest bending-ratio coupling is between 10° and 30°. In contrast, the fiber orientation of 0° and 45° resulted in 0 coupling ratio, which indicates that there is no coupling between bending and torsion stiffness. Hence, in this study, the chosen composite laminate configurations are [30°]$_4$ and [45°]$_4$ that respectively represent the sample with the existence and non-existence of the bending-torsion coupling parameters.

Table 2: Parameters of [D] as defined from CLT

Fiber Orientation (θ°)	D_{11} (GPa.mm^3)	D_{12}	D_{16}	D_{22}	D_{26}	D_{66}
[0$_4$]	1.88	0.113	0.000	1.88	0.00	0.0576
[5$_4$]	1.85	0.138	0.141	1.85	-1.41	0.0825
[10$_4$]	1.78	0.209	0.265	1.78	-2.65	0.0154
[15$_4$]	1.67	0.319	0.357	1.67	-3.57	0.0264
[20$_4$]	1.54	0.454	0.406	1.54	-4.06	0.0399
[25$_4$]	1.39	0.597	0.406	1.39	-4.06	0.0542
[30$_4$]	1.26	0.732	0.357	1.26	-3.57	0.0677
[35$_4$]	1.15	0.842	0.265	1.15	-2.65	0.0787
[40$_4$]	1.08	0.913	0.141	1.08	-1.41	0.0858
[45$_4$]	1.05	0.938	0.000	1.05	0.00	0.0883

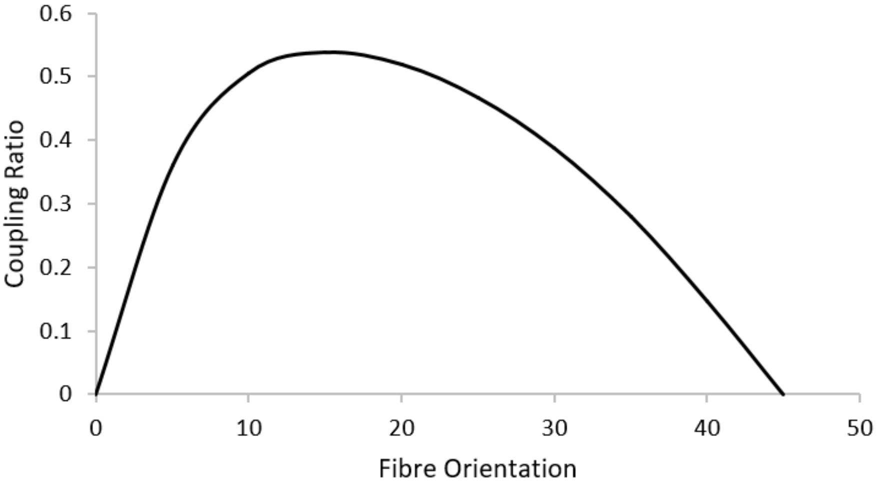

Figure 2: Bending-torsion coupling ratio at different fibre orientation

In the experimental tests, the composite flat wing models are installed on the test rig and placed in the wind tunnel test section. An accelerometer is used in this study to measure the acceleration of the wing root in three axes of direction: the x- and y- coordinate axes and direction of the air stream, which are indicated in Figure 3. During the experimental tests, wind tunnel velocity is systematically increased from an initial value of 0 m/s to the final value of 20 m/s. The occurrence of flutter speed is carefully monitored, which signifies the onset of oscillatory and vibratory behavior in the wing model's structure. Therefore, during the flutter point, the accelerometer data will show significant changes in the voltage in the three different axes. To ensure precision and minimize experimental errors, the composite wing model undergoes three consecutive test iterations. This approach aims to enhance accuracy and reduce potential reading errors during the experiment.

Figure 3: Experimental set-up in the test section of the wind tunnel

It should be noted that the experimental test rig is constructed to serve as a horizontal and rigid apparatus, acting as the support structure for the composite wing to replicate its behavior during flight. It is made as a rigid holder with various sections that may be adjusted to hold the wing at various angles of attack. This configuration facilitates the passage of air through the wing model, thus demonstrating the phenomenon of flutter that occurs when the wind velocity reaches the flutter limit.

3. Results and Discussion

Through the geometrical and material setup in the pre-processing of the ABAQUS software, the free vibration analysis of the composite flat wing structure with the laminate stacking sequences of $[\theta]_4$ different fiber orientations are conducted. From Table 3, the first four structural natural frequencies for each fiber orientation are presented. On the other hand, Figure 4 and Figure 5 show the variations of the first four structural natural frequencies for the composite flat wing models with $[30°]_4$ and $[45°]_4$ laminates, respectively. For the composite flat wings with $[30°]_4$ and $[45°]_4$ laminates, it can be observed from Figure 4 and Figure 5 that the first three frequencies are dominated by the bending displacements, and the fourth frequency displays torsional displacements. Afterwards, the experiment is conducted to validate the data presented in Table 3 using the test setup shown in previous Figure 3. The experimental results obtained from the accelerometer are plotted in Figure 6 and Figure 7 for the composite flat wing models with $[30°]_4$ and $[45°]_4$ laminates, respectively.

Table 3: Natural frequencies of composite flat wing at different fibre orientations

Fibre Orientation	**Natural Frequency (rad/s)**				**Flutter Speed**
	1	**2**	**3**	**4**	
$[30°]_4$	2.275	14.391	43.103	49.434	16.0 m/s
$[45°]_4$	2.0647	13.175	39.867	59.699	19.2 m/s

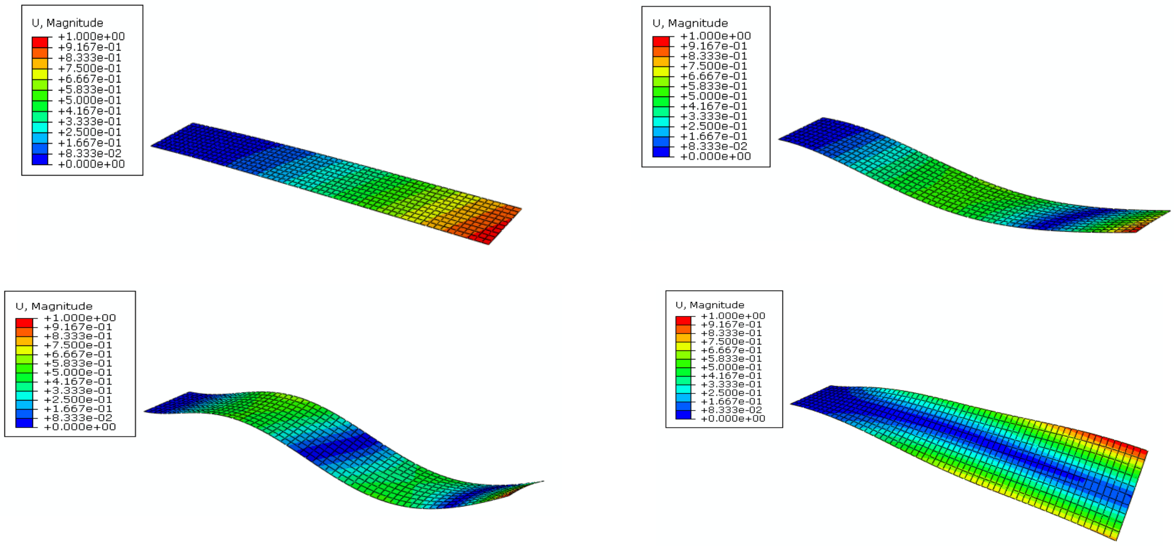

Figure 4: Natural frequencies and mode shapes of composite flat wing with $[30°]_4$

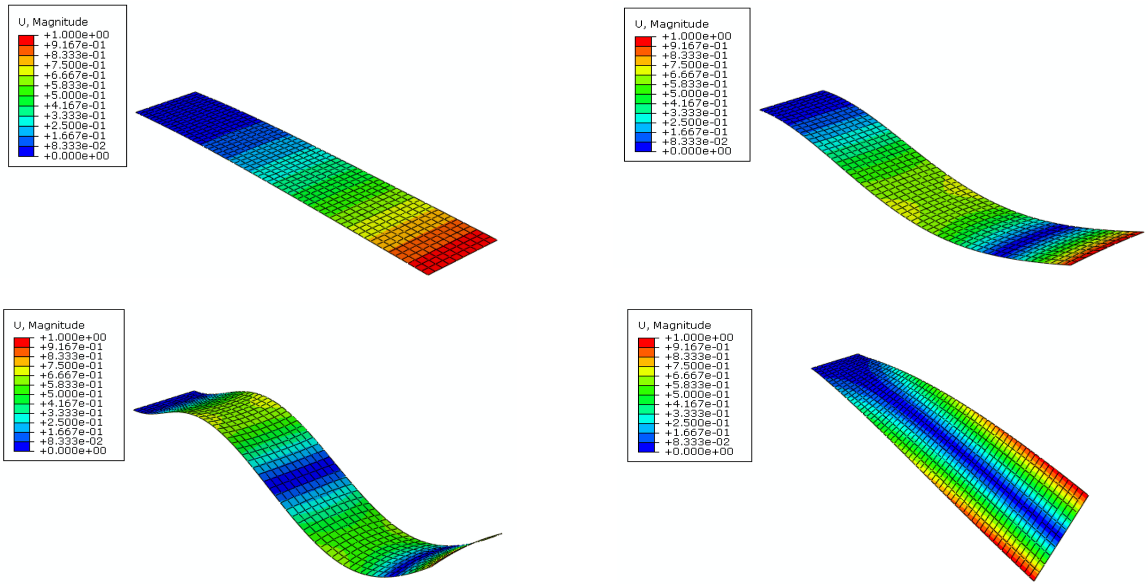

Figure 5: Natural frequencies and mode shapes of composite flat wing with $[45°]_4$

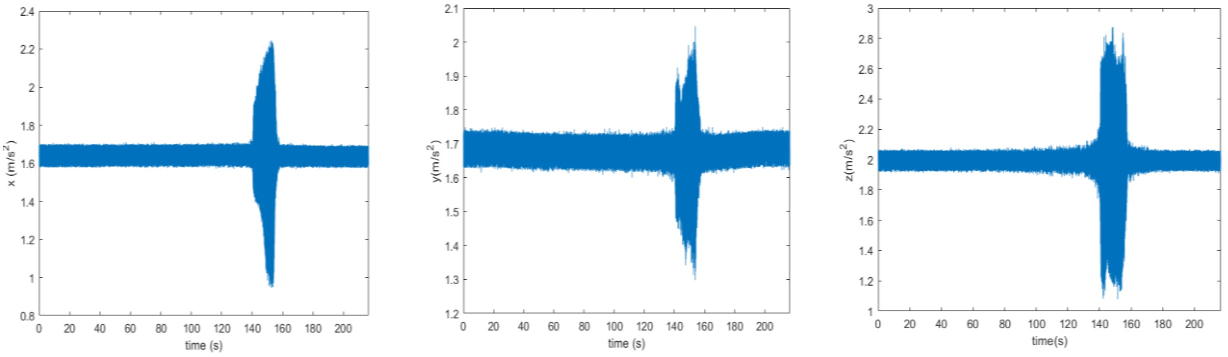

(a) (b) (c)

Figure 6: Accelerometer data for wing model with $[30°]_4$ laminate: (a) x-axis, (b) y-axis, (c) z-axis

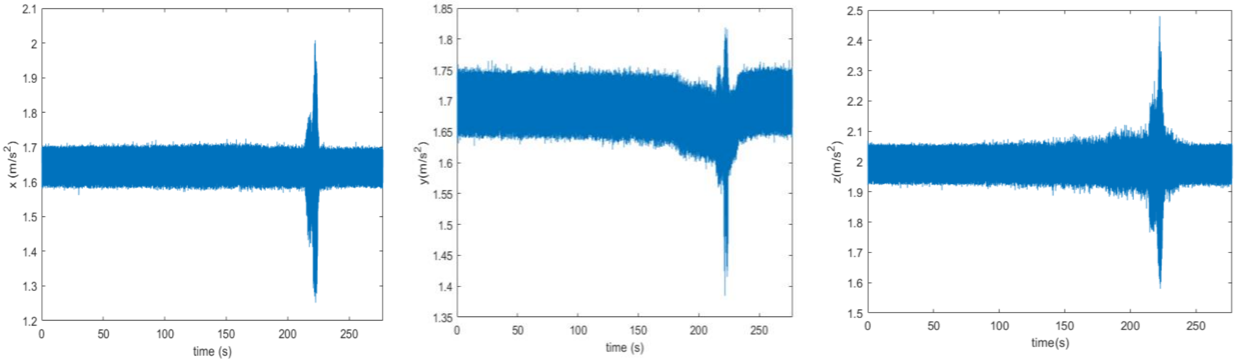

(a) (b) (c)

Figure 7: Accelerometer data for wing model with [45°]$_4$ laminate: (a) x-axis, (b) y-axis, (c) z-axis

The experimental results are recorded through an accelerometer sensor and video to observe the changes in displacement of the x-, y- and z- axes, as well as the vibration of the wing model when the wind tunnel's speed is increased from 0 m/s until the wing model starts to oscillate. Note that Figure 6 and Figure 7 present the recorded data along (a) x-axis, which is the chordwise direction of the wing, (b) y-axis, which is the spanwise direction, and (c) z-axis, which is the vertical direction. The peaks in the amplitude from Figures 6(a) and 6(b) indicate the occurrence of structural deformation in x- and y-axes while the amplitude peaks in Figure 6(c) implies vertical oscillations. It should be noted that the peak in Figure 6(c) coincides with the oscillations observed in the x- and y- axes, which shows that the wing model undergoes a complex three-dimensional motion as it reaches the flutter point within a time range between 140 to 160 seconds into the experiment, equivalent to 12.5 m/s wind speed. Similarly, from Figures 7(a), 7(b) and 7(c), the amplitude peaks of the x-, y- and z- axes can be observed between the time range of 210 to 240 seconds, equivalent to 19.0 m/s wind speed, which indicates the structural deformation has occurred at the flutter point.

The recorded data from the accelerometers and video footage is compared and correlated in order to obtain the flutter speed point. The result comparison between the experimental testing and the finite element analysis (FEA) are presented in Table 4. It shows clearly that the flutter speeds predicted by the FEA is higher than the experimental tests. For instances, the difference between the results of FEA and experiment tests for wing model with [30°]$_4$ laminate is 21.8% and [45°]$_4$ is 5.2%, respectively. This situation is likely due to the FEA software used in this study may not have fully captured the effects of bending-torsional coupling, which could be significantly for certain fiber orientations. Besides that, the result obtained has also shown that the flutter speed is significantly affected by the existence of bending-torsion coupling, which promotes the flutter to occur at a lower speed. This finding is also in line with the observation made by Mitra et al. [12]. Moreover, in comparison to pure laminate [45°]$_4$ that has the highest torsional rigidity [13], the flutter speed can be further increased up to 46%.

Table 4: Comparisons of flutter speed

Composite wing model	**Flutter Speed (m/s)**	
	FEA	**Experiment**
[30°]$_4$	16.0	12.5
[45°]$_4$	19.2	18.2

4. Conclusion

From the results and discussion of this studies, it is known that the cross-coupling parameters are important to be determined before conducting the analysis on composite laminates. The influence of this cross-coupling parameter can be seen during the analysis of structural natural frequencies and their mode shapes, especially for the fiber orientation between 5° and 40°. Higher cross-coupling parameters indicate a high coupling between bending and torsion. The inclusion of bending-torsion coupling has a significant effect on the structural vibration, which is shown to lead towards reduction of up to 31.3% of flutter speed as demonstrated from the difference in the results obtained from FEA and experimental analysis. It can be concluded that, to avoid the flutter phenomenon from occurring on composite wing at low speeds, it is necessary to design the composite wing with the inclusion of 45° plies as to enhance the torsional rigidity of the composite wing.

Acknowledgement

The authors highly acknowledge Universiti Teknologi Malaysia and Ministry of Education Malaysia for financial support to implement this research through UTMFR grant (Q.J130000.3851.21H92) and FRGS grant (R.J130000.7851.5F517).

References

[1] A. R. Collar, 'The Expanding Domain of Aeroelasticity', The Aeronautical Journal, vol. 50, no. 428, pp. 613-636, 1946.

[2] I. E. Garrick and W. H. Reed III, 'Historical Development of Aircraft Flutter', Journal of Aircraft, vol. 18, no. 11, pp. 897-912, 1981.

[3] J. R. Wright and J. E. Cooper, Introduction to Aircraft Aeroelasticity and Loads, John Wiley & Sons, 2008.

[4] M. S. Othman, O. T. Chun, M. Y. Harmin and F. I. Romli, 'Aeroelastic Effects of a Simple Rectangular Wing-Box Model with Varying Rib Orientations', IOP Conference Series: Materials Science and Engineering, vol. 152, no. 1, 012009, 2016.

[5] T. Farsadi and J. J. Hasbestan, 'Calculation of Flutter and Dynamic Behavior of Advanced Composite Swept Wings with Tapered Cross Section in Unsteady Incompressible Flow', Mechanics of Advanced Materials and Structures, vol. 26, no. 4, pp. 314-332, 2019.

[6] T. K. Jun, M. Y. Harmin and F. I. Romli, 'Aeroelastic Tailoring of Composite Wing Design Using Bee Colony Optimisation', Applied Mechanics and Materials, vol. 629, pp. 182-188, 2014.

[7] S. G. P. Castro, T. A. M. Guimarães, D. A. Rade and M. V. Donadon, 'Flutter of Stiffened Composite Panels Considering the Stiffener's Base as a Structural Element', Composite Structures, vol. 140, pp. 36-43, 2016.

[8] G. A. Georghiades and J. R. Banerjee, 'Flutter Prediction for Composite Wings using Parametric Studies', AIAA Journal, vol. 35, no. 4, pp. 746-748, 1997.

[9] S. J. Hollowell and J. Dugundji, 'Aeroelastic Flutter and Divergence of Stiffness Coupled, Graphite/Epoxy Cantilevered Plates', Journal of Aircraft, vol. 21, no. 1, pp. 69-76, 1984.

[10] T. A. Weisshaar and R. J. Ryan, 'Control of Aeroelastic Instabilities Through Stiffness Cross-Coupling', Journal of Aircraft, vol. 23, no. 2, pp. 148-155, 1986.

[11] A. Attaran, D. L. Majid, S. Basri, A. S. Mohd Rafie and E. J. Abdullah, 'Structural Optimization of an Aeroelastically Tailored Composite Flat Plate Made of Woven Fiberglass/Epoxy', Aerospace Science and Technology, vol. 15, no. 5, pp. 393-401, 2011.

[12] A. Mitra and A. Chakraborty, 'Multi-objective Optimization of Composite Airfoil Fibre Orientation Under Bending–Torsion Coupling for Improved Aerodynamic Efficiency of

Horizontal Axis Wind Turbine Blade', Journal of Wind Engineering and Industrial Aerodynamics, vol. 221, 104881, 2022.

[13] A. Viglietti, E. Zappino and E. Carrera, 'Free Vibration Analysis of Variable Angle-Tow Composite Wing Structures', Aerospace Science and Technology, vol. 92, pp. 114-125, 2019.

JOURNAL OF
AEROSPACE SOCIETY MALAYSIA

ARTICLE

EXPERIMENTAL ASSESSMENT OF PROPELLER-DOWNWASH EFFECTS ON THE WING'S AERODYNAMIC CHARACTERISTICS AT LOW REYNOLDS NUMBER

Muhammad Aqil Karimi Mohd Sabri [1], Mohamad Izzat Truna [2], Mohd Rashdan Saad [2], Norzaima Nordin [2], Muhammad Amirul Adli Nor Zaidi [1] and Baizura Bohari [2,*]

1. Kulliyyah of Engineering, International Islamic University Malaysia, Kuala Lumpur, Malaysia.
2. Department of Aeronautic Engineering and Aviation, Faculty of Engineering, Universiti Pertahanan Nasional Malaysia, Kuala Lumpur, Malaysia.

*Correspondence: baizura@upnm.edu.my

Abstract: Unmanned aerial vehicles (UAVs) and micro air vehicles (MAVs), which are often referred to as drones, are among the advancing technologies that are utilized to secure remote surveillance. The propeller technology used by these aircraft has a considerable impact on their wing's aerodynamics. It has been shown that the propeller slipstream affects the pressure distribution over the wing surfaces in both chordwise and spanwise directions, influencing the distribution of wing loading especially during low-speed cruising. This study is done to examine the effects of propeller slipstream at low Reynolds numbers on several airfoils, namely NACA 0012, NACA 4415 and NACA 6712, concentrating on four key factors: type of airfoil, propeller diameter, propeller speed and distance between the propeller and the rectangular wing. Specifically, in the context of employing propellers for UAV applications, the goal is to evaluate if these parameters result in improvements and to analyze their impacts on lift, drag and lift-to-drag ratio. On the whole, the results imply that the propeller effect reduces lift and drag on most parameters discussed. However, the lift-to-drag ratio appears to increase on specific parameters. In this case, reducing the distance between the wing and the propeller leads to noticeable improvement in the lift-to-drag ratio. However, if the distance becomes extremely small, lift-to-drag ratio starts to decrease again.

Keywords: propeller slipstream; propeller diameter; propeller speed; propeller distance; NACA airfoils

1. Introduction

The application trend of Unmanned Aerial Vehicles (UAVs) in the industry has shown a significant increase, especially in recent years whereby they are mostly used for both civilian and military purposes [1]-[2]. UAVs often operate at low Reynolds number. In the aviation and aircraft operation, turboprop aircraft uses propellers as their source of thrust and it has been shown that employing propellers in air vehicles yields excellent performance at low speeds region [3]. The propeller functions by creating thrust through differences in pressure between the front and rear surfaces of its airfoil-shaped blades. It has been highlighted that the propeller diameter is a crucial factor in propeller design. Through a numerical analysis utilizing STAR CCM+, the effects from varying the propeller diameter on the thrust (speed) performance have been investigated. The findings indicate that larger diameters lead to decreased drag and this is attributed to the heightened thrust generated, resulting in reduced induced drag. It has been affirmed in several studies that enlarging the propeller diameter will enhance the wing's lift-to-drag ratio [5]-[7]. Furthermore, the research demonstrates that smaller diameters yield higher lift-to-drag ratio at high angles of attack, whereas larger diameters exhibit superior lift-to-drag ratio at lower angles of attack for the same pitch.

Furthermore, the separation between the propeller and wing is also a critical factor that influences the generated lift and drag forces. Previous research study has indicated that the absence of a propeller significantly impacts aerodynamic properties, with the specific effects will vary based on the propeller's placement [8]. The study emphasizes the importance of the propeller-to-wing distance in preserving the aerodynamic qualities, highlighting that increasing this distance with multiple propellers can lead to a reduction in drag. Moreover, another study has explored how the vertical distance (Z position) between the propeller and the wing impacts the lift coefficient [9]. In this study, it has been found that increasing the vertical distance between the wing and the propeller results in a decrease in lift coefficient.

It should be noted that previous researches are predominantly focused on propeller effects at high Reynolds number levels in aircraft applications. Studies on the propeller diameter, distance and analysis typically center around single propeller and distributed propeller (DP) aircraft. Further research needs to be conducted on propeller applications in UAVs to enhance the understanding and also evidence for sustainable aviation practices.

2. Methodology

The objective of this research is to examine how the slipstream from a propeller impacts the wings of an aircraft with various types of airfoils under low Reynolds number conditions. This study analyzes the influence of the propeller on lift and drag coefficients across different airfoil designs, the impact of the distance between the propeller and the airfoil, the effects of varying propeller diameters on lift and drag, and the consequences of using different propeller RPMs on the aircraft performance. The tests have been carried out in the low-speed LW-9300R Subsonic Wind Tunnel, employing the three-force balance setup. This wind tunnel utilizes open-loop suction to generate simulated wind, reaching speeds up to 105 m/s. It is an open-loop suction-type wind tunnel with dimensions of 0.3 m (W) x 0.3 m (H) x 1.0 m (L). The considered range of Reynolds number (Re) in this study is between 5×10^4 to 9×10^4, which is defining the low Re regime. The propeller's RPM is adjusted between 1200 and 1800 to prevent stall, and accommodate the small-scale airfoil model within the wind tunnel. The distance between the propeller blade and the airfoil is varied from 4 cm to 7 cm.

Three airfoils used in this experiment are NACA 0012, NACA 4415 and also NACA 6712. The computer-aided design (CAD) model of these airfoils is developed using SOLIDWORKS software and then sliced using ULTIMAKER Cura. The detailed coordinates and data for these airfoils are provided in Table 1.

Table 1: Airfoil profile coordinates

Airfoil profile	Maximum thickness (%)	Maximum camber (%)	Maximum camber position (%)	Chord line (mm)	Wing span (mm)
NACA 0012	12.2	0	0.0	155	250
NACA 4415	15.0	4	40.2	155	250
NACA 6712	12.0	6	70.0	155	250

In the meantime, the propeller mounting setup comprises two distinct sections: the baseplate and the propeller mounting. The propeller mounting's center of radius is positioned 16 cm above the wind tunnel's ground level to align with the airfoil's center of gravity. The baseplate is also generously sized to match with the width of the wind tunnel's test section, ensuring stability during the testing. Both the propeller mounting and baseplate are manufactured using similar process as the airfoil models. Notably, the baseplate is designed with 100% infill to enhance its weight and strength, ensuring it can withstand the wind speeds within the wind tunnel. Furthermore, an Arduino Nano microcontroller is applied to control the speed of the propeller in revolutions per minute (RPM). The RPM value is displayed on an LCD screen. The Arduino Nano reads input from the brushless DC motor (BLDC) GT2215 and uses PID (Proportional-Integral-Derivative) control to regulate the speed. A YUMO E6B2-CWZ3E Rotary Encoder is also incorporated for speed measurement and control. Table 2 provides the details on the components used in this setup while Figure 1 shows visual representation of the propeller setup.

Table 2: List of components and their function

Components	Functions
LCD Display unit	Display propellers' RPM
Control Switch	A potentiometer that controls the propellers' RPM
Arduino Nano	Microcontroller (programmed with PID controller).
YUMO E6B2-CWZ3E Rotary Encoder	Use to measure rotation position. Arduino Nano collects the rotation position data and converts it to rotation speed in RPM.
Brushless DC motor (BLDC)	A motor that is used to rotate the propeller. BLDC is connected to the encoder by a shaft for PID purposes.
Electronic Speed controller (ESC)	To control the speed of the brushless motor (no feedback). The ESC will receive PWM from Arduino Nano to spin the BLDC. ESC is also used to supply 5V to Arduino Nano.
LiPo Battery	Acts as a power source of the whole system. It supplies voltage to all the electronic components in the circuit ranging from 6.4V to 8.4V.

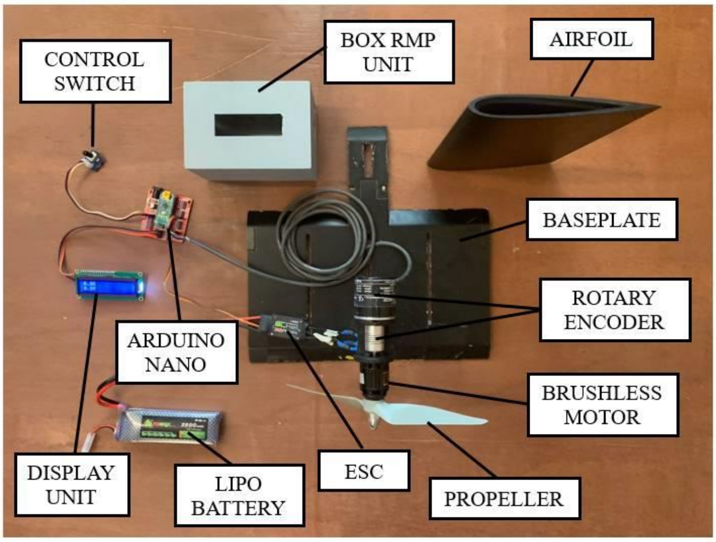

Figure 1: Propeller setup components

The configuration of the propeller arrangement in the wind tunnel is illustrated in Figure 2. The propeller's rotation speed can be adjusted externally using the control switch and it is monitored via the display unit.

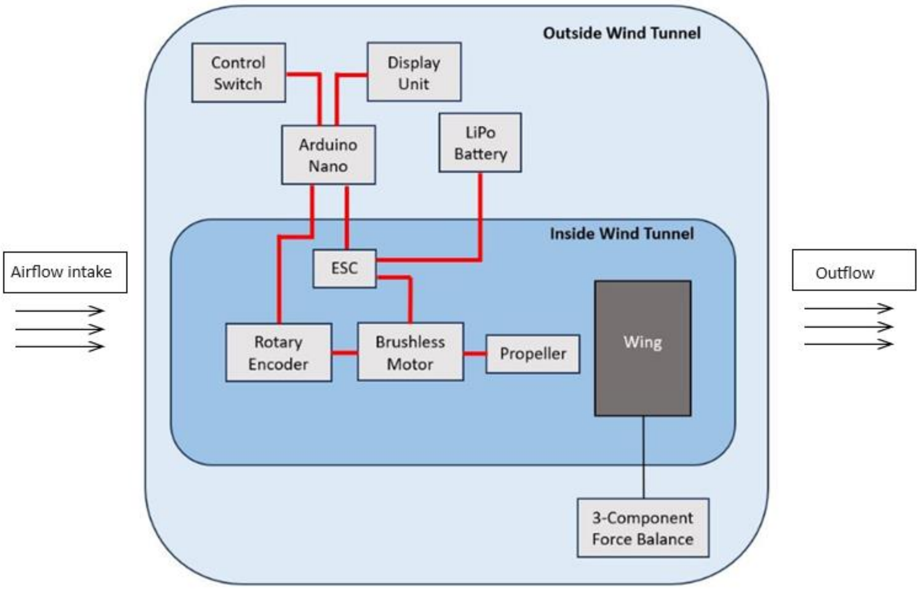

Figure 2: Diagram of the setup inside the wind tunnel

As mentioned before, this study aims to investigate four main factors: the impact of various airfoil types when subjected to the propeller effect, the influence of different propeller diameters, the effects of varying propeller speeds (measured in RPM) and the consequences of altering the distance between the propeller blade and the wing. The propeller configuration is positioned at a 5-cm distance from the airfoil, which is affixed to the force balance as depicted in Figure 3. The RPM meter and Arduino Nano circuit are located outside of the wind tunnel for monitoring and control purposes.

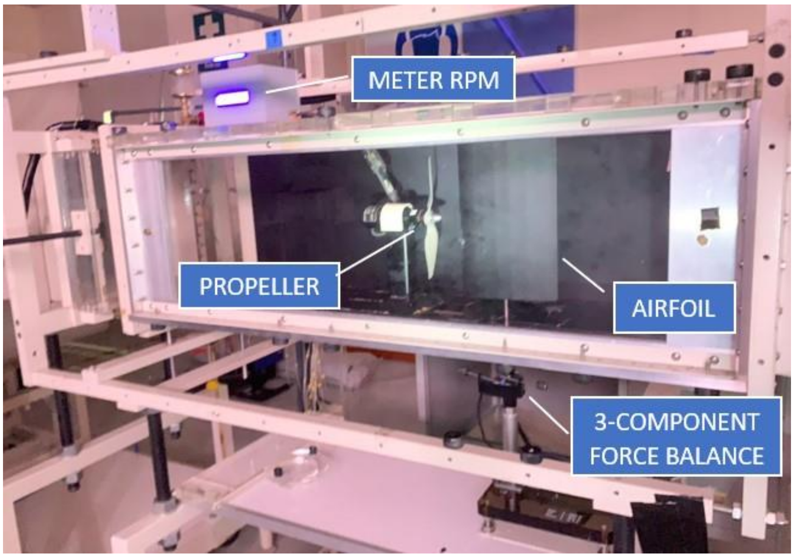

Figure 3: Experimental setup of propeller and airfoil

The variables considered in this experiment are the airfoil design, propeller size, propeller rotation speed (revolutions per minute or RPM), propeller position and Reynolds number. In each part of the experiment, Reynolds number is maintained as the primary constant parameter. Table 3 tabulates the constant parameters used throughout the experiment while Table 4 lists the dependent and independent variables for all the experiments performed.

Table 3: Constant parameters

Variable (units)	**Values**
Reynolds number	5.0×10^4, 6.0×10^4, 7.0×10^4, 8.0×10^4, 9.0×10^4
Angle of attack	0 degree
Wing chord line (mm)	155
Wing span (mm)	250

Table 4: Variables of the experiment

Independent Variables		**Dependent Variables**	
Airfoil Types	NACA 0012 NACA 4415 NACA 6712	**Wing Forces**	C_L C_D
Propeller Speed (RPM)	1200 RPM 1400 RPM 1600 RPM 1800 RPM		
Propeller Diameter (diameter x pitch)	7 x 6 inch 8 x 6 inch 9 x 6 inch	**Wing Performance**	C_L/C_D
Propeller Distance (cm)	4 cm 5 cm 6 cm 7 cm		

The first part of this study is to investigate the performance of the considered three airfoil types in terms of their suitability for flight operations, focusing on lift and drag coefficients. For this experiment, the propeller speed is set to 1200 RPM, propeller distance is set to 5 cm and propeller diameter is set to 7 x 6 inch. The airfoil models used in this experiment are shown in Figure 4. Based on the results of this first part of the study, the airfoil that exhibits the best performance as measured by its lift-to-drag ratio (C_L/C_D) is selected to be used in the subsequent part of the experiment.

NACA 6712 **NACA 4415** **NACA 0012**

Figure 4: Models for the three considered types of NACA airfoils

Next, only the selected best airfoil type is used in the second part of this study, which involves the experimental testing with varying propeller diameters while maintaining the propeller distance and RPM as in the previous experimental setup (i.e. propeller speed is 1200 RPM and propeller distance is 5 cm). The goal of this second part of the investigation is to analyze the impact of different propeller diameters on the resultant lift and drag. Three propeller diameters are considered in this study as illustrated by the models depicted in Figure 5, namely 7 x 6 inch, 8 x 6 inch and 9 x 6 inch (i.e. the first number in the dimension denotes the propeller's diameter in inches while the second number refers to the pitch). The propeller model is affixed to the brushless DC motor (BLDC) shaft and consistent RPM is maintained throughout the duration of the experiment.

In the meantime, the third part of this experimental investigation is to study the impact of varying propeller speeds (RPM) on the selected best airfoil type. For this experiment, propeller distance is set to 5 cm and propeller diameter is set to 7 x 6 inch while the RPM is varied from 1200 up to 1800. The influence of RPM on the propeller's effectiveness in relation to the airfoil is assessed to understand its effect on lift and drag coefficients. RPM control is achieved through an Arduino Nano microcontroller programmed to regulate the BLDC input. RPM output is monitored and filtered using an encoder, with results displayed on the LCD screen. A potentiometer is utilized to adjust the RPM.

Lastly, the final part of this study is intended to examine the impact of varying the distance between the propeller blade and the wing, ranging from 4 cm to 7 cm, on lift and drag of the selected best airfoil type. This parameter is crucial in enhancing or diminishing the aerodynamic forces. To conduct this experiment, the propeller mounting is adjusted according to the specified distances. The experimental setup for the distance variation is illustrated in Figure 6. In this experiment, the propeller speed is set to 1200 RPM and propeller diameter is set to 7 x 6 inch.

Figure 5: Three different propeller diameters

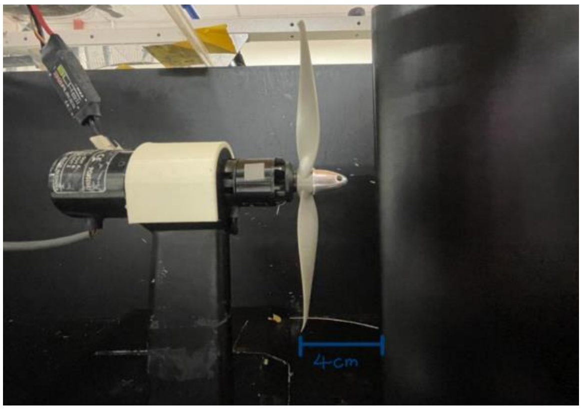

Figure 6: Setup for propeller distance effects

For all stages of this experimental study as described above, the same testing procedure is applied. The metal bar with a slotted wing is affixed using hot glue and clay, and then is connected to the three-force balance component to maintain the airfoil structure's stability during experiment. The propeller base is secured to the wind tunnel’s floor upstream of the wing. All small electronic components and connections are positioned outside the wind tunnel and secured with tape to minimize any obstruction to the propeller or wing from the freestream flow. The distance between the propeller and wing can be adjusted by moving the propeller rig pole and adjusting the baseplate as needed. The propeller's desired radius is secured to the motor using an Allen key to prevent detachment during high-speed testing. The propeller is centered to ensure it is in a cruise condition. Once the propeller radius, distance between the propeller and wing, and also wing alignment have been established, the propeller speed is adjusted by manipulating the potentiometer until the desired value is displayed on the LCD screen. Subsequently, the freestream velocity within the wind tunnel is regulated by adjusting the wind tunnel’s frequency. A brief pause of 5-10 seconds is implemented to ensure precise readings are captured. Following this, the wind tunnel frequency is set to zero and the propeller speed is also brought to a halt. This sequence is then replicated for various speeds. The propeller is then removed and replaced with a different diameter propeller for subsequent experiments, following the same procedure. This process is also repeated for different distance configurations. Each experiment is conducted thrice to gather data for calculating the average results.

3. Results and Discussion

The first experimental stage is focused on examining the aerodynamic performance of the different considered airfoil types: NACA 0012, NACA 4415 and NACA 6712. As shown in Figure 7, the graph depicts the relationship between drag coefficient (C_D) and Reynolds number (Re) that is obtained from the experiment. The graph's findings highlight that NACA 0012 exhibited the lowest drag compared to the other airfoils. Additionally, it demonstrates an increasing trend in drag as Re is increased. Based on this, NACA 0012 airfoil can be recommended for flying at low Reynolds numbers due to its superior C_D performance. For NACA 6712 and NACA 4415 airfoils, their trends are quite similar. However, at lower Reynolds numbers, NACA 4415 airfoil has displayed lower drag when compared to NACA 6712. Both airfoils are therefore advised for flights within the Reynolds number range of 5 x 10^4 to 6 x 10^4 and the range of 8 x 10^4 to 9 x 10^4. For these two airfoils, operating outside of the regions would result in increased drag, which will diminish the aircraft's overall performance. All in all, when considering only the drag coefficient, NACA 0012 proves to be an optimal choice for minimizing drag, particularly when factoring in the propeller's effects.

Meanwhile, the lift coefficient vs Re plot, as depicted in Figure 8, also offers valuable insights. It reveals a consistent trend in lift coefficient across all airfoils. Notably, NACA 6712 and NACA 4415 airfoils have exhibited an increasing C_L as Re is increased. In contrast, NACA 0012 airfoil has displayed a decreasing C_L as Re increased. Among these three airfoils, NACA 6712 airfoil has stood out with an exceptional C_L performance compared to the other two airfoils. Consequently, NACA 6712 emerges as an excellent choice for achieving high lift when combined with the propeller's influence.

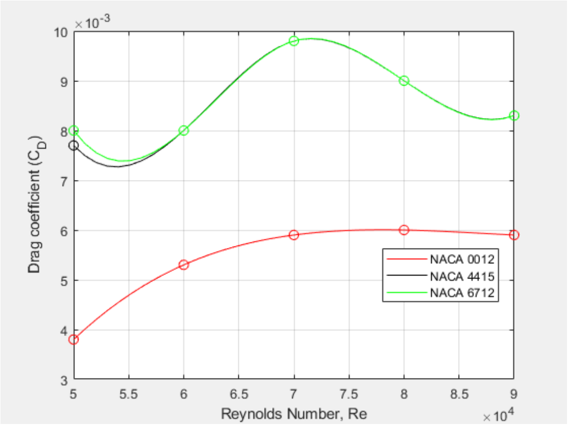

Figure 7: Drag coefficient, C_D against Re for different airfoil types

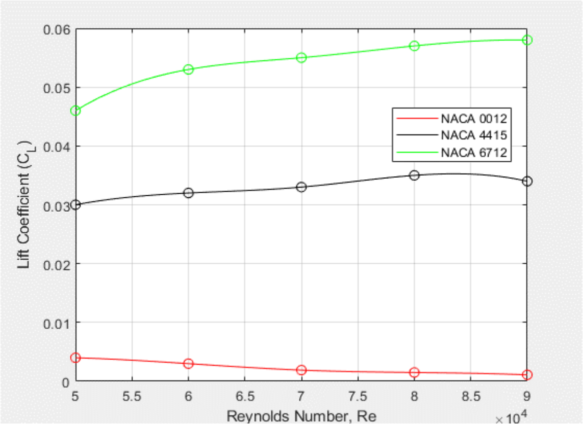

Figure 8: Lift coefficient, C_L against Re for different airfoil types

Furthermore, the C_L/C_D graph in Figure 9 shows that NACA 0012 airfoil exhibits a declining trend in terms of C_L/C_D as Reynolds number (Re) increases. This pattern suggests that the NACA 0012 airfoil might not be well-suited for flight operations. On contrary, both NACA 0012 and NACA 6712 airfoils show identical C_L/C_D ratios at Re = 5 x 10^4. However, it is advisable to avoid flight within the Re range of 6 x 10^4 to 8 x 10^4 as the C_L/C_D ratio decreases within this region for both airfoils. Beyond this range, the flight performance for both airfoils generally remains satisfactory, except for the NACA 6712 airfoil that is not recommended for low Re (i.e. 5 x 10^4 to 5.5 x 10^4). Furthermore, it is important to note that NACA 6712 airfoil consistently achieves a higher maximum C_L/C_D ratio compared to NACA 4415 airfoil, indicating that NACA 6712 offers superior C_L/C_D performance for the flight operations when considering the propeller effect. In summary, NACA 6712 emerges as the most efficient NACA airfoil configuration for flight operations, primarily due to its consistently high C_L/C_D performance, and it is selected as the best airfoil type to be used for the experiments in the following stages of this study.

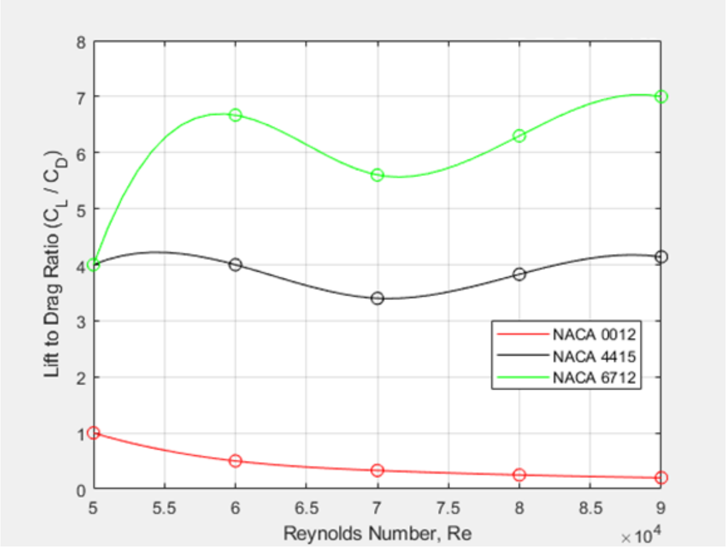

Figure 9: Lift-to-drag ratio, C_L/C_D against Re for different airfoil types

The second part of this experimental study us investigating the impact of propeller diameter on the wing's aerodynamic properties. The NACA 6712 airfoil, which is chosen based on the results from previous experiment, is used. The resultant C_D versus Re graph for the different propeller diameters is shown in Figure 10. It can be observed that C_D consistently decreases across all diameter configurations, within the Re ranges of 5 x 10^4 to 6 x 10^4 and 8 x 10^4 to 9 x 10^4, signifying excellent performance for flight operations within these regions. Hence each configuration should operate outside these specified regions as doing so will increase drag. Comparing the three propeller diameters, it is observed that for the lower Re range of 5 x 10^4 to 6 x 10^4, propeller diameter 7 x 6 inch has displayed considerably greater C_D than propeller diameter 9 x 6 inch. Conversely, within the Re range of 8 x 10^4 to 9 x 10^4, propeller 7 x 6 inch has demonstrated the lowest C_D while propeller 8 x 6 inch has exhibited the highest C_D. Apart from the mentioned regions, all diameter configurations displayed a consistent and similar trend with minimal differences in terms of C_D.

Figure 11 illustrates the C_L versus Re graph for the various propeller diameters. Across all diameter configurations, a consistent trend emerges, marked by an increasing C_L with respect to Re. This pattern indicates that C_L tends to be higher at higher Re values. However, it is important to note that operating within the lower Re range (i.e. 5 x 10^4 to 6 x 10^4) is discouraged due to significantly lower C_L values within this region. Apart from this specific region, all diameter configurations display a notable increase in C_L as Re increases, affirming the relationship between C_L and higher Re values. Notably, at Re of 8 x 10^4 to 9 x 10^4, the C_L for propeller diameter 8x6 surpasses that of other configurations. Meanwhile, propeller diameter 7 x 6 inch boasts the highest C_L at regions outside of 8 x 10^4 to 9 x 10^4. In terms of the C_L parameter, propeller diameter 7 x 6 inch appears to be a favorable choice for the flight operations, particularly at low Re values, as it consistently yields high C_L values across most Re regions below 9 x 10^4.

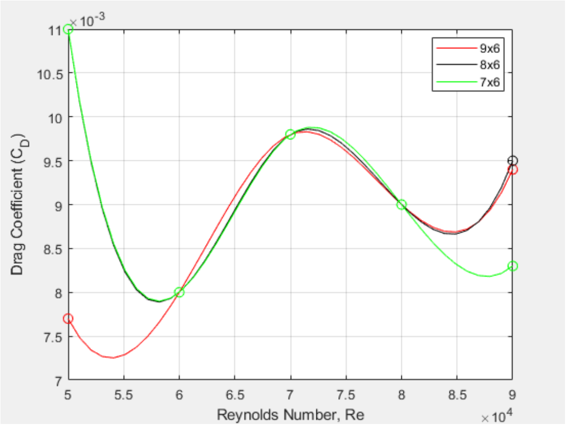

Figure 10: Drag coefficient, C_D against Re for different propeller diameters

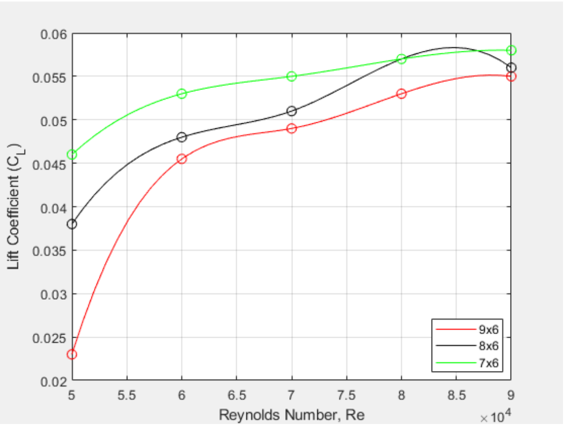

Figure 11: Lift coefficient, C_L against Re for different propeller diameters

Figure 12 displays the C_L/C_D data and related graph for various propeller sizes. Among the three propeller diameter configurations (7 x 6 inch, 8 x 6 inch, and 9 x 6 inch), specific regions stand out as favorable for flight operation. The regions include Re range between 5.5 x 10^4 to 6.5 x 10^4 and between 8 x 10^4 to 9 x 10^4, where C_L/C_D values exhibit a positive trend, signifying both increasing values and high performance. Thus, it is recommended to conduct the flight operations using any of these three propeller diameter configurations within these specified regions. Among the propeller diameters, 9 x 6 inch yields the highest C_L/C_D values in the recommended flight regions compared to others. On the other hand, the regions outside the mentioned ranges should be avoided for flight operations as they exhibit lower C_L/C_D values, which is indicative of diminished performance. Furthermore, it is observed that, as the propeller diameter increases, the propeller's effect becomes more pronounced, particularly at lower Re values for C_D. This aligns with previous research, which suggests that drag decreases with increasing diameter in low Re conditions (i.e. 5 x 10^4 to 6 x 10^4) [10]. As a result, the propeller's impact provides positive feedback for C_D at lower Re while being less effective at higher Re. The propeller with the lowest C_D at low Re (i.e. 5 x 10^4 to 6 x 10^4) shows that drag decreases with increasing diameter [4]. As the propeller diameter decreases, the wing's lift also rises [11]. It can be observed that increasing the propeller diameter will enhance the influence of propeller slipstream, which has a positive effect on C_D at low Re but a negative effect on C_L at most Re regions below 9 x 10^4. To conclude, propeller diameter of 7 x 6 inch is the most effective diameter for flight configuration since it has the highest C_L/C_D.

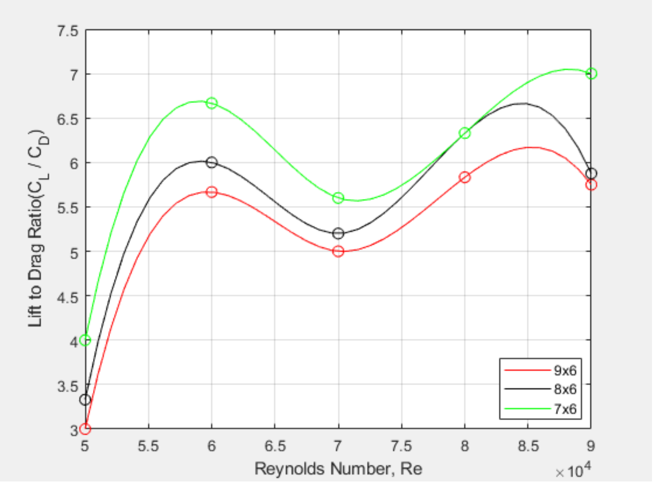

Figure 12: Lift-to-drag ratio, C_L/C_D against Re for different propeller diameters

Moreover, in the third stage of this experimental study, the effect under investigation is the impact of propeller speed on its aerodynamic characteristics. In this case, the speed is manipulated by using a potentiometer, which transmits the input to the Arduino Nano. Subsequently, a PID process is applied and the RPM value is displayed on the LCD screen. The propeller speed is varied as 1200 RPM, 1400 RPM, 1600 RPM and 1800 RPM. Figure 13 illustrates the graph of C_D versus Re for different RPM. At RPM of 1600, the drag coefficient exhibits a decrease within the Re range between 5 x 10^4 to 5.5 x 10^4 and between 8 x 10^4 to 9 x 10^4. Flying operations in these regions are recommended for the 1600 RPM setting since the drag coefficient is lower than in other regions. Conversely, for RPM settings of 1200 and 1800, flying within the Re range between 5.5 x 10^4 to 6.5 x 10^4 and between 8 x 10^4 to 9 x 10^4 is advisable. However, within the Re range between 8 x 10^4 to 9 x 10^4, the drag coefficient for 1200 RPM is significantly lower than 1800 RPM. To summarize, avoiding flying operations within the Re range of between 6 x 10^4 to 8 x 10^4 is advisable for all settings of the propeller speed. C_D increases significantly in this region compared to other regions below Re of 9 x 10^4.

Meanwhile, Figure 14 illustrates the relationship between lift coefficient and Re for various RPM settings. Each RPM setting exhibits a distinct C_L trend. Notably, as RPM increases, the trend becomes less stable and less distinct. Both 1400 RPM and 1600 RPM exhibit increasing trends but their C_L values in the lower Re range are considerably lower than those at 1200 RPM. As RPM increases further, C_L decreases across all Re values. At 1800 RPM, C_L decreases notably in the Re range between 5 x 10^4 to 6.5 x 10^4, indicating that the airfoil starts to stall at higher Re when the RPM is elevated. Additionally, C_L decreases in the Re range between 8 x 10^4 to 9 x 10^4. In summary, the configuration with low RPM settings consistently produces higher and more stable C_L values.

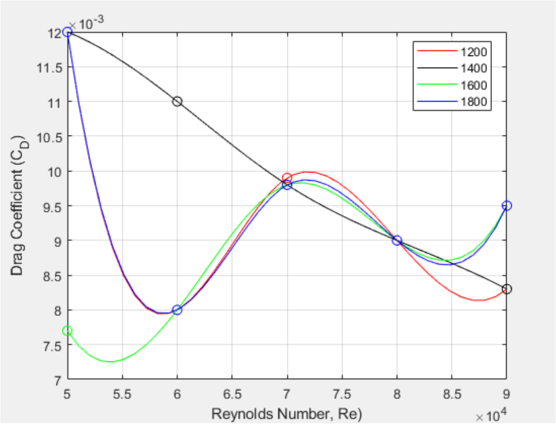

Figure 13: Drag coefficient, C_D against Re for different propeller speeds

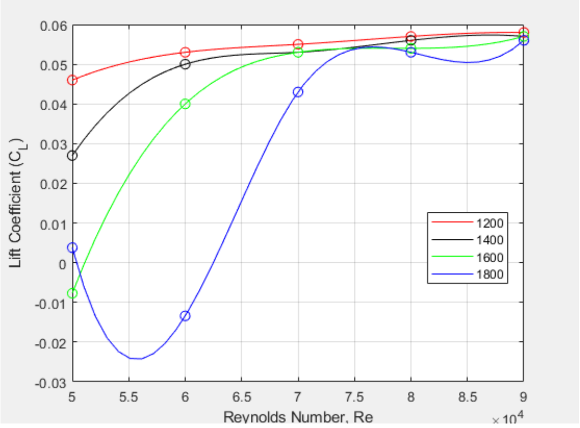

Figure 14: Lift coefficient, C_L against Re for different propeller speeds

As shown in Figure 15, all RPM settings exhibit consistent performance level of C_L/C_D values and trends within Re range between 7 x 10^4 to 8 x 10^4. In Re range between 5 x 10^4 to 7 x 10^4, the C_L/C_D trends for the RPM settings of 1200, 1400 and 1600 exhibit noticeable and consistent increase with the rising Re. Notably, among these settings, the 1200 RPM arrangement produces the greatest C_L/C_D. On the other hand, at RPM 1800, the C_L/C_D first decreases from Re of 5 x 10^4 to 5.5 x 10^4 before rising to Re of 7 x 10^4. This trend indicates that when the RPM value rises, flight operation performance gets unpredictable and the system becomes unstable. Within Re range between 8 x 10^4 to 9 x 10^4, the 1200 RPM and 1400 RPM settings demonstrate an increase in C_L/C_D as Re increases. On contrary, for the 1600 RPM setting, C_L/C_D increases until Re of 8.5 x 10^4 and then decreases until Re of 9 x 10^4. Notably, the 1800 RPM setting experiences a decline in C_L/C_D until Re of 8.5 x 10^4 and then witnesses an increase until Re of 9 x 10^4. In summary, these observations underscore that the higher RPM settings introduce more significant fluctuations and reduced stability in flight operation performance, particularly within transition regions between different Reynolds numbers. A more comprehensive examination involving Particle Image Velocimetry (PIV) could be done to provide valuable insight into the flow characteristics of the same configuration across various RPM settings. Among the considered RPM configurations, RPM of 1200 emerges as the most optimal choice since it consistently yields the highest C_L/C_D across all Re ranges. This is aligned with the findings from another study that also shows an increase in RPM corresponds to increase in thrust coefficient, signifying that higher RPM levels intensify the propeller's influence on the airfoil [12].

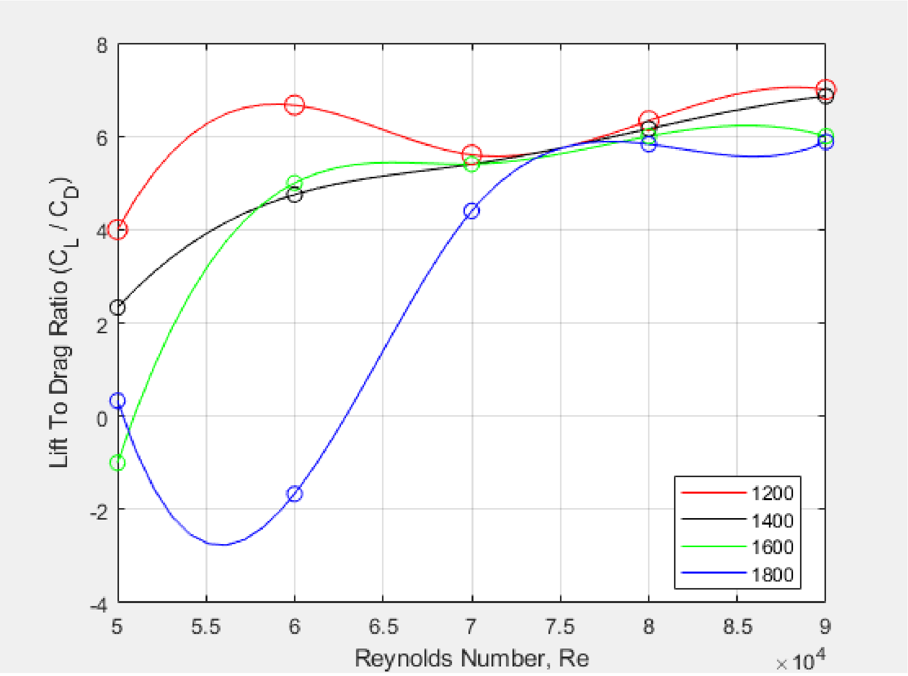

Figure 15: Lift-to-drag ratio, C_L/C_D against Re for different propeller speeds

Last but not least, the final experimental stage explores how the airfoil's aerodynamic characteristics are affected when the distance between the propeller blade and the airfoil is altered. This investigation examines distances ranging from 4 cm to 7 cm. It has been indicated that this distance parameter plays pivotal role in distributed propulsion systems, exerting large influence on aerodynamic performance compared to the number of propellers [8]. Therefore, investigating the impact of distance assumes significant importance in this context. Figure 16 illustrates the C_D versus Re graph for various distances. Interestingly, the 4 cm and 5 cm configurations exhibit no discernible difference in C_D. This outcome can be attributed to the limited scope of the small distance range explored in this experiment. For both 4 cm and 5 cm configurations, conducting flight operations within the Re regions between 6 x 10^4 to 8 x 10^4 and at Re of 9 x 10^4 is advisable. This is due to the low C_D values within this range, contributing to improved aircraft performance. Moving beyond this region for propeller distances of 4 cm and 5 cm is not recommended as it leads to increased drag, thereby diminishing the flight performance. It is also interesting to note that, at the 6 cm distance, C_D exhibits lower values at lower Re region (i.e. between 5 x 10^4 to 6 x 10^4) and Re = 9 x 10^4. Based on this analysis, it is evident that the closer the distance between the propeller and the airfoil, the lower the drag produced, especially at lower Re.

Additionally, Figure 17 shows the plot of C_L versus Re for various propeller distances. Across all configurations, the graph exhibits a consistent increasing trend in C_L with increasing Re. Notably, at the distance of 7 cm for all Re regions, the highest maximum C_L is attained compared to other settings. In the range of Re between 5 x 10^4 to 6 x 10^4, the 6 cm distance configuration boasts the highest C_L among the considered options while 5 cm distance outperforms 4 cm distance in terms of C_L. With increasing Re up to 7 x 10^4, the 4 cm configuration experiences significantly higher C_L than 5 cm, whereas 7 cm maintains the highest C_L. As Re continues to rise to Re of 9 x 10^4, the lift of the 5 cm configuration once again increases, surpassing the C_L of the 4 cm configuration. However, for 6 cm and 7 cm, the C_L remains consistent. This analysis underscores that the furthest distance between the propeller results in the highest C_L. Conversely, as propeller distance decreases, C_L decreases and exhibits more fluctuations, rendering it less stable. Consequently, the configuration with the furthest distance proves to be optimal for generating high lift. It is advisable for aircraft to operate within the Re range of 7.5 x 10^4 to 9 x 10^4 since during this region, the lift generated is greater compared to the other regions, indicating excellent performance in flight operations.

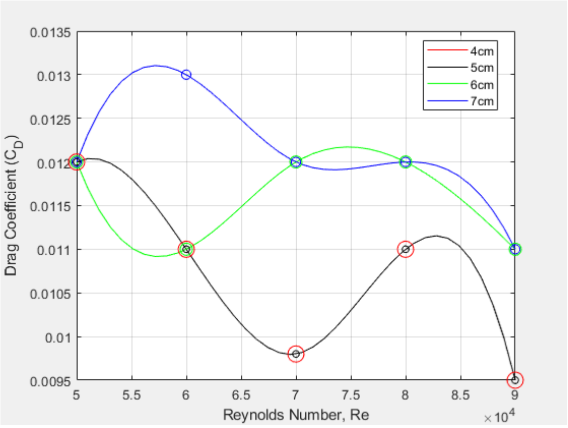

Figure 16: Drag coefficient, C_D against Re for different propeller distances

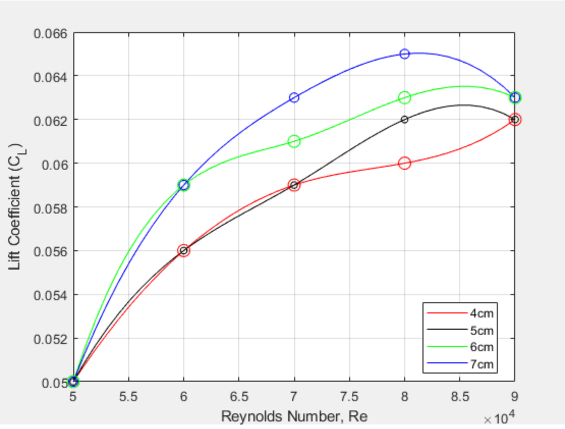

Figure 17: Lift coefficient, C_L against Re for different propeller distances

The plot of lift-to-drag ratio, C_L/C_D against Re, as depicted in Figure 18, reveals interesting insights. Initially, the configurations with 4 cm and 5 cm distances exhibit similar trends from Re range between 5 x 10^4 to 7 x 10^4. However, as Re continues to increase, the C_L/C_D for the 5 cm configuration surpasses that of the 4 cm configuration significantly. Consequently, it is advisable for both configurations to avoid flying within the Re range between 5 x 10^4 to 6.5 x 10^4 since the flight operation's performance in this region is suboptimal. In contrast, Re of 7 x 10^4 and 9 x 10^4 emerge as the optimal Re regions for both configurations in terms of flight operations. At these two points, higher C_L/C_D values are attained, indicating improved performance. In the meantime, the performance for 6 cm distance configuration exhibits significant variations across different Re regions. It experiences substantial increase in C_L/C_D at lower Re values (i.e. from 5 x 10^4 to 6 x 10^4), followed by a decrease until Re of 7.5 x 10^4, and then another increases up to Re of 9 x 10^4. On the other hand, the 7 cm configuration demonstrates favorable flight operation at Re range between 7 x 10^4 to 9 x 10^4, producing higher C_L/C_D values. On the contrary, the 7 cm configuration experiences a sharp decrease in C_L/C_D at lower Re values (i.e. from 5 x 10^4 to 6 x 10^4). On the whole, the analysis suggests that the 6 cm configuration performs exceptionally well at lower speeds (lower Re). In contrast, the 5 cm configuration is well-suited for higher Re operations below Re of 9 x 10^4. Reducing the distance between the propeller and the airfoil reduces drag [2]. This phenomenon occurs because the effect of the propeller slipstream is much stronger at closer distances. However, it is essential to note that reducing the distance also reduces C_L. Therefore, it becomes evident that the propeller slipstream's effect simultaneously reduces lift and drag. In distance configuration, the analysis indicates that the 5-cm distance setting offers the most optimal performance in C_L/C_D. This favorable outcome may be attributed to the more significant reduction in drag compared to the decrease in lift, suggesting that the propeller positively impacts the aerodynamic characteristics when considering different distance configurations.

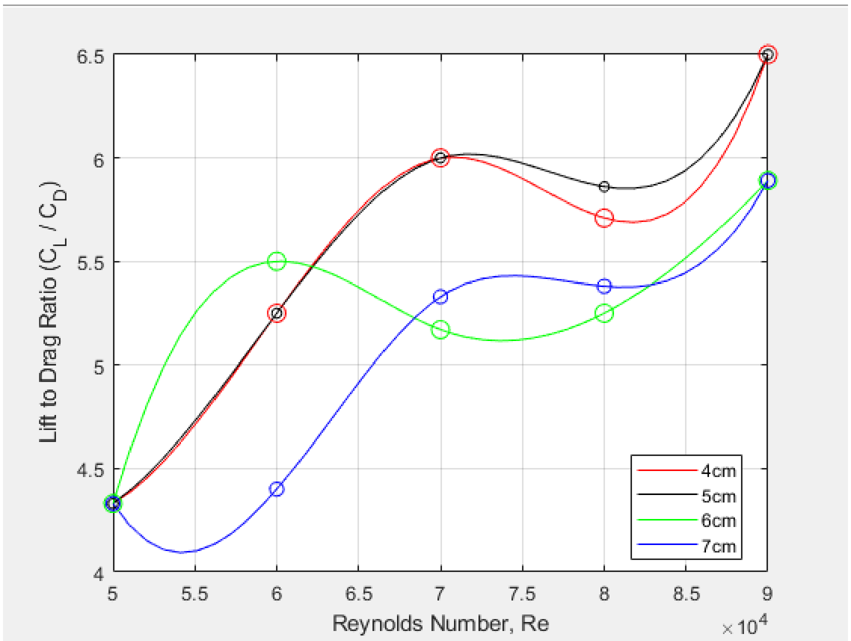

Figure 18: Lift-to-drag ratio, C_L/C_D against Re for different propeller distances

4. Conclusion

The impact of propeller slipstream on the aerodynamic performance varies depending on specific parameters. Positioning the propeller at a moderate distance, rather than too close, notably enhances the airfoil's lift-to-drag ratio. According to the results, the optimal configuration for propeller analysis at low Re involves small 7 x 6 inch diameter, low RPM setting of 1200 and 5 cm distance. Consequently, this configuration proves highly suitable for UAV applications due to its minimal space requirements for propeller diameter and low RPM, which eliminates the need for high-power supply. Moreover, the shorter distance reduces the overall size. While the propeller effect reduces both lift and drag, the drag reduction is more prominent and greatly improves the lift-to-drag ratio of the airfoil, especially when discussing the effect of distance.

Acknowledgement

The authors fully acknowledge the Ministry of Higher Education (MOHE), Malaysia and Universiti Pertahanan Nasional Malaysia for financial support to implement this research through the GPJP grant, UPNM/2020/GPJP/TK/11.

References

[1] R. W. Deters, G. K. A. Krishnan and M. S Selig, 'Reynolds Number Effects on the Performance of Small-Scale Propellers', Presented at 32nd AIAA Applied Aerodynamics Conference, Atlanta, USA, June 2014.

[2] K. Wang, Z. Zhou, X. Zhu and X. Xu, 'Aerodynamic Design of Multi-Propeller/Wing Integration at Low Reynolds Numbers', Aerospace Science and Technology, vol. 84, pp. 1-17, 2019.

[3] K. R. Moore and A. Ning, 'Distributed Electric Propulsion Effects on Existing Aircraft Through Multidisciplinary Optimization', Presented at AIAA/ASCE/AHS/ASC Structures, Structural Dynamics, and Materials Conference, Kissimmee, USA, January 2018.

[4] P. D. Vecchia, D. Malgieri, F. Nicolosi and A. De Marco, 'Numerical Analysis of Propeller Effects on Wing Aerodynamic: Tip Mounted and Distributed Propulsion', Transportation Research Procedia, vol. 29, pp. 106-115, 2018.

[5] C. Mingzhi, L. Kun, W. Chunqiang, W. Jingbo and Q. Zijie, 'Research on the Distributed Propeller Slipstream Effect of UAV Wing Based on the Actuator Disk Method', Drones, vol. 7, 2023.

[6] O. N. Vinogradov, A. V. Kornushenko, O. V. Pavlenko, A. V. Petrov, E. A. Pigusov and T. T. Ngoc, 'Influence of Propeller Diameter Mounted at Wingtip of High Aspect Ratio Wing on Aerodynamic Performance', Journal of Physics: Conference Series, vol. 1959, no. 1, 012051, 2021.

[7] F. Makino and H. Nagai, 'Propeller Slipstream Interference with Wing Aerodynamic Characteristics of Mars Airplane at Low Reynolds Number', Transactions of the Japan Society for Aeronautical and Space Sciences, vol. 12, 2014.

[8] D. Keller, 'Towards Higher Aerodynamic Efficiency of Propeller-Driven Aircraft with Distributed Propulsion', CEAS Aeronautical Journal, vol. 12, no. 4, pp. 777-791, 2021.

[9] G. J. Resende, V. Malatesta, M. C. Savio and B. M. Castro, 'Wing's Aerodynamic Characteristics due to Distributed Propulsion Over the Wingspan', Journal of the Brazilian Society of Mechanical Sciences and Engineering, vol. 45, no. 9, 2023.

[10] H. Zhu, Z. Jiang, H. Zhao, S. Pei, H. Li and Y. Lan, 'Aerodynamic Performance of Propellers for Multirotor Unmanned Aerial Vehicles: Measurement, Analysis and Experiment', Shock and Vibration, vol. 2021, pp. 1-11, 2021.

[11] E. A. Marcus, R. de Vries, A. R. Kulkarni and L. L. Veldhuis, 'Aerodynamic Investigation of an Over-the-Wing Propeller for Distributed Propulsion', Presented at AIAA Aerospace Sciences Meeting, Kissimmee, USA, January 2018.

[12] Z. Czyż, P. Karpiński, K. Skiba and M. Wendeker, 'Wind Tunnel Performance Tests of the Propellers with Different Pitch for the Electric Propulsion System', Sensors, vol. 22, no. 1, 2021.

REVIEW OF THE STOL CHANNEL-WING AIRCRAFT DESIGN AND DEVELOPMENT

Meriwon Surtan@John [1], Abd. Rahim Abu Talib [1], Ezanee Gires [1] and Mohd Faisal Abdul Hamid [1,*]

1. Department of Aerospace Engineering, Universiti Putra Malaysia, Serdang, Selangor, Malaysia.

*Correspondence: mohd_faisal@upm.edu.my

Abstract: Custer channel wings, sometimes referred to as channel wings, have become a viable solution to control aerodynamic flow and enhance air vehicle performance. This design breakthrough, which dates back to the 1920s, involves redefining the traditional wing shapes into semi-circular or U-shaped configurations to promote suction effect that improves lift generation. Although channel wings present an exciting opportunity to transform the aircraft design, there are still unanswered questions, especially on the best way to integrate them into the contemporary aircraft. In order to fill these gaps, this study examines the viability of channel wing technology and evaluates its possible effects on the operation and design of the commercial aircraft. Through the new developments in materials science and engine technology, previous limitations related to the channel wing designs including weight penalties and drag inefficiencies can be overcome.

Keywords: short-haul flights; channel-wing; aerodynamic design; U-shaped wing; STOL

1. Introduction

The increasing expansion of global economy has increased demands for air transport, necessitating faster long-distance delivery and more efficient people movement [1]. Flight operations are scheduled to restart when the globe recovers from the epidemic in 2020 (as illustrated in Figure 1) and the forecasts suggest an increase in air travel demands, accompanied by increase in the number of passengers [2]. In accordance with the United Nations, more than half of the global population currently resides in cities, the number projected to reach 60% by 2030 [3]. Despite the presence of numerous conventional aircraft in daily operation, the aviation industry needs a paradigm shift [4]-[5]. Conventional aircraft contribute significantly to air traffic congestion, necessitating substantial improvements in this domain. The focus should be on advancing Vertical Takeoff and Landing (VTOL) and Short Takeoff and Landing (STOL) capabilities to address this challenge effectively [6]-[8].

In line with this, revolutionizing the conventional wing is critical in influencing the future of aircraft design, providing a plethora of options for addressing current issues particularly those experienced in short-haul flights. The existing wing design's restrictions limit the ability to maximize its lift generation. Integrating active flow control technology stands out as a viable alternative for improving the wing's aerodynamic performance [9]. Implementing such innovations unlocks the possibility for enhanced lift generation and efficiency, opening the path for substantial advancements in aviation. Furthermore, it can be noted that efficiency, affordability and compact size are key considerations that are highly valued in the aviation community. To achieve this objective requires an aircraft with exceptional aerodynamic performance. Previous studies have shown that channel-wing aircraft have great potential in effectively addressing these challenges. The channel wing configuration has proven to be an excellent choice for short-haul flights, with the ability to perform VTOL and STOL maneuvers [10]-[11].

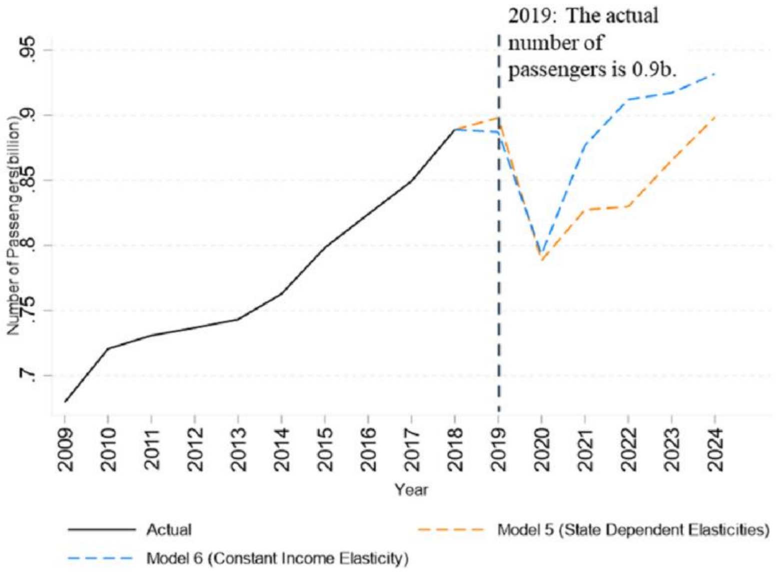

Figure 1: Air travel recovery in the next 5 years (2019–2025) [2]

2. Concept of Channel-Wing

The first concept of channel-wing configuration, which is depicted in Figure 2, came out in 1920s and pioneered by Willard Custer. In 1940s, the concept started receiving serious attention and as shown in Figure 3, further design improvements were made in 1950s where the wing was constructed in the shape of a hemisphere or a U-shaped channel [12]. By combining a fixed wing component with the U-shaped channel, the channel-wing is formed. The propulsion system is positioned near the trailing edge of the channel, allowing the air to flow over the wing's surface. The channel wing works by using the slipstream induced increased dynamic pressure to create lift, which is then directed through the channel to provide additional lift and thrust [13]. At the lower speeds or when stationary, the high-speed rotating propeller blades create a low-pressure region inside the channel, generating differential pressure on the upper and lower surfaces of the wing. This results in a significant amount of lift that surpasses what the conventional wings can achieve [14]. On contrary, at higher speeds, the advantage of the channel-wing becomes very limited. Nevertheless, the combined projected areas of the channel-wing and fixed-wing components can provide sufficient lift to keep the aircraft airborne [12].

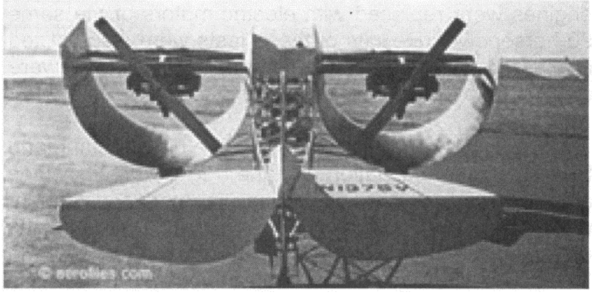

Figure 2: The CCW-2 series channel-wing aircraft [13]

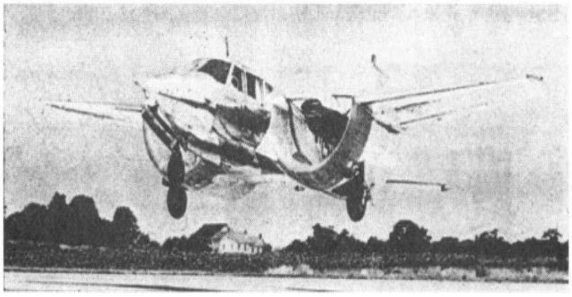

Figure 3: The CCW-5 series channel-wing aircraft [13]

In general, the channel-wing is a form of aircraft's wing that generates lift by utilizing Coanda effect and having a U-shaped wing that increases the surface area of the wing. A jet of air is forced across the curved surface of the wing to provide lift in the channel-wing [13]. The Coanda effect is also utilized in various aircraft designs such as the Coanda-1910 plane, which utilize it to generate lift and propulsion [15]. Many improvements have been tested on the channel-wing design to fully utilize both the U-shape and the aileron design, one of which is the pneumatic (blown) technology as shown in Figure 4. It can be noted that this technology has been shown to be capable to undertake various functions including high lift, drag reduction and better control, along with fitting blown components incorporated into the design to perform a range of functions that most of the time omit the use of moving parts on the outer surfaces of the aircraft [15]. At the moment, it has low blowing mass fluxes but recent research aims to lower this further. These efforts are important to produce much better effects. On the other hand, ideas such as giving pulsing blow on the pneumatic systems will help to deplete the blowing mass flow and subsequently lead to significant improvement in usable lift. In addition, it has been shown that takeoff or landing speeds and distances will significantly drop. This pneumatic solution can assist in addressing the issues of extreme STOL technology by providing an efficient and effective way of attaining high lift and control without the need of complicated and heavy mechanical systems [15].

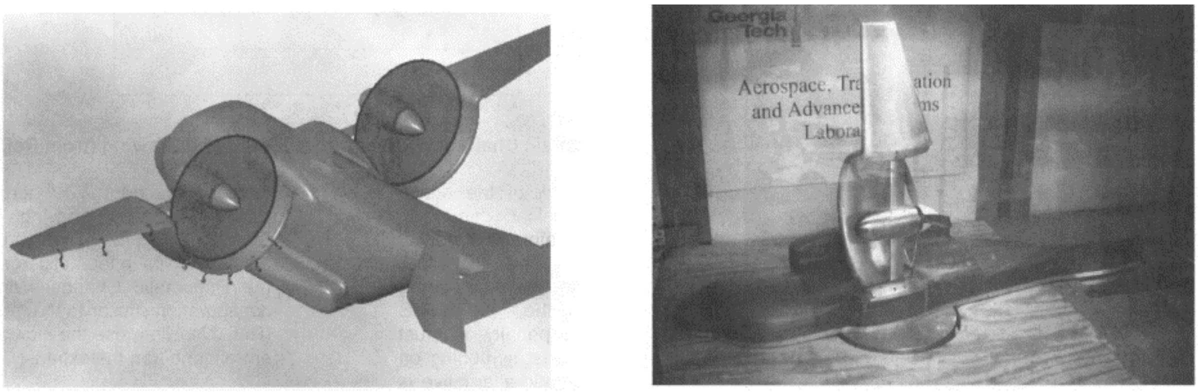

Figure 4: Conceptual pneumatic channel wing and semi-span model in GTRI [15]

In a conducted study on the channel-wing aircraft design, it has been found that despite successful demonstration of its advantages for take-off and landing performance, this aircraft design faces several challenges in meeting the certification requirements for general aviation use [13]. Furthermore, in terms of climbing and high-speed capabilities, it is also evident that the channel-wing aircraft design has lower performance in comparison to the available certified twin-engine aircraft designs in the current market. From the business perspective, the channel-wing aircraft design's modest improvement in field length performance is overshadowed by its numerous flight-related drawbacks and associated expenses. On a different note, it has been demonstrated that by angling the wing at approximately 40 degrees, it could potentially achieve vertical take-off and landing (VTOL) capabilities [15]. This has the potential to create more options for individuals or airlines dealing with limited runway lengths. It is crucial to consider the potential of channel-wing aircraft in modern context, particularly in addressing commercial and military needs like the V-22. The channel-wing aircraft might be able to offer intriguing lifting capabilities with higher cruise speeds at a lower weight/cost compared to the V-22 [16]-[17].

While the traditionally designed straight-wing aircraft have excelled in numerous aspects since their introduction, they do also come with certain trade-offs, particularly in terms of lift-to-drag ratios and stall characteristics. It is worth noting that the aircraft design and certification have a long history dating back to the early 1900s and the straight-wing concept has been the prevailing choice for the fixed-wing aircraft [18]. Considering this, there is a compelling need for more research and development efforts in the branch of channel-wing design [19]-[21]. Such endeavors have a potential to significantly contribute to the advancement of aviation technology, potentially leading to practical applications and influencing the design of future aircraft [22]-[23]. This exploration aligns with ongoing advancements in materials, propulsion and aerodynamics, offering the prospect of mitigating some of the existing limitations in aircraft design while maintaining the popularity of fixed-wing aircraft for various aviation applications.

3. Early Development of Channel-Wing

In 1925, Willard Custer was inspired to innovate the new channel-wing design after witnessing the natural phenomenon where a strong wind lifted the roof of a barn. He then realized that the high speed of the wind flow could create minimal pressure above the roof while the inner pressure stayed constant, resulting in the roof being blown off. This same theory could be applied to aircraft wings to generate lift, even when the aircraft is stationary. After conducting some research, Custer built his first U-shaped aircraft wing model in 1928, which he patented in 1929 [24]. In 1942, Custer further refined the design and created the Custer Channel-Wing 1 (CCW-1), which he flew for the first time. The CCW-2 model followed with even greater features such as the ability to perform almost vertical take-offs and leave the ground like a helicopter. Custer received positive feedback about his new wing design, particularly from military departments. In 1954, he began producing another remarkable series, known as CCW-5, which unfortunately turned out to be the last in the CCW series.

Custer's initial patent featured an aircraft with a conventional fuselage and tail, to which a channel-wing powered by the same engine and featured a variable pitch layout for forward flight performance. By placing the propellers close to the channel boundaries, the tip losses were minimized. This deliberate positioning of the propeller at the back of the wing, close to the trailing edge, was a key component of Custer's innovation, as shown in Figure 5. This unusual positioning created the suction effect over the channel, increasing lift. It was also recommended that the leading-edge propeller's blades feathered to reduce landing speed and Custer had an idea to regulate the feathering by working the engine and other controls. By exploiting the channel-wing's greater lift capability, the upwardly extending semi-cylindrical channel improved the jet aircraft’s take-off and landing stability. One of the design aims was to reduce take-off and landing distance [25]. On the whole, the development of the idea of super circulation led to the successful testing of the Custer’s channel-wing design [26].

Figure 5: The propeller location for CCW-5 aircraft [24]

In 1953, the work by Jerome Pasamanick became the crucial stepping stone in the evolution of the channel-wing aircraft [27]. This study provided empirical evidence on possibilities of the configuration by subjecting the Custer’s channel-wing aircraft to few extensive tests in full-scale tunnels. The channel-wing design has actively changed since the 1950s and numerous significant improvements have already been achieved in the design's aerodynamics and control features over time.

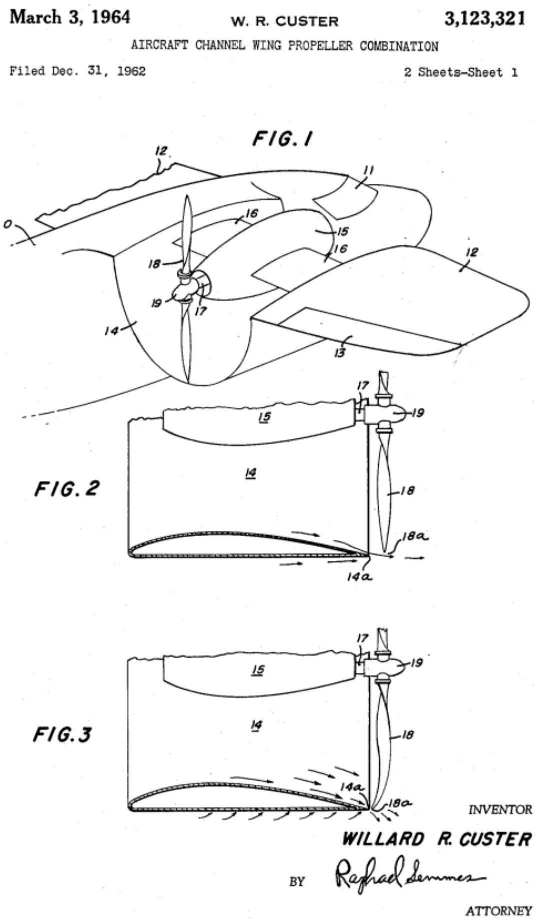

March 3, 1964 W. R. CUSTER 3,123,321
AIRCRAFT CHANNEL WING PROPELLER COMBINATION
Filed Dec. 31, 1962 2 Sheets-Sheet 1

INVENTOR
WILLARD R. CUSTER
BY Raphael Semmes
ATTORNEY

Figure 6: Willard Custer's patent (US3123321 A) that was published in 1964 [12]

Willard Custer came up with the original idea for the channel wing, which has its roots in the artistic milieu of the 1940s. The pusher system with the propeller placed at the trailing edge of the wing served as the basis for this configuration. The wing itself had peculiar half-cylindrical shape that was specifically designed to put the propeller tip near to the trailing edge. This structure became the foundation for the preliminary tests and studies that facilitated the channel-wing design to be further developed [28]-[29]. Without question, the channel wing is special experiment that pushed the limits of aviation innovation. It ventured to break from the tradition and contest the then accepted standards of aircraft design. The channel wing became a representation of bold exploration in aviation, thanks to the creative thoughts, thorough testing, and a dedication to pushing the boundaries of technology [30].

Figure 7: Original CCW-5 aircraft [31]

By utilizing the accelerated air near the propulsive device, which is often a propeller, lift force can be created even when the aircraft's forward velocity is minimal or zero. The main premise of the Custer channel wing is that lift is generated by the relative air velocity, not by the speed of the aircraft. Based on the preliminary assessment, propeller-based systems demand that the propeller be positioned near the back of the channel and have little space between the tips of the propeller and the duct. The airflow through the duct/propeller can generate lift force if the cross section of the duct has an airfoil shape with chord near to radius [31]-[32]. It is worth to note the improvements of the channel wing design made by Rhein Flugzeugbau. In less than ten years, he produced two successful powered gliders, the Sirius 1 and Sirius 2, as well as a twin-seat light aircraft, Fanliner, which made its first flight at the end of 1973 [33]. The Fanliner's success prompted the construction of its sister plane, Fantrainer, using the same concept while also testing the rotary engine's evolution, which is characterized by shifting standards brought on by the energy conservation and also the raw material considerations on 1977. The rotary engine's high power density, made possible by its kinematics and unrestricted ports, offers the advantages in size and speed. A 4-rotor, 1500 HP engine with the potential military and commercial applications is the recent development. The versatility of the rotary engine onto Fantrainer suggests further investigation in other areas [33]. Figure 8 shows both the Fanliner and Fantrainer aircraft.

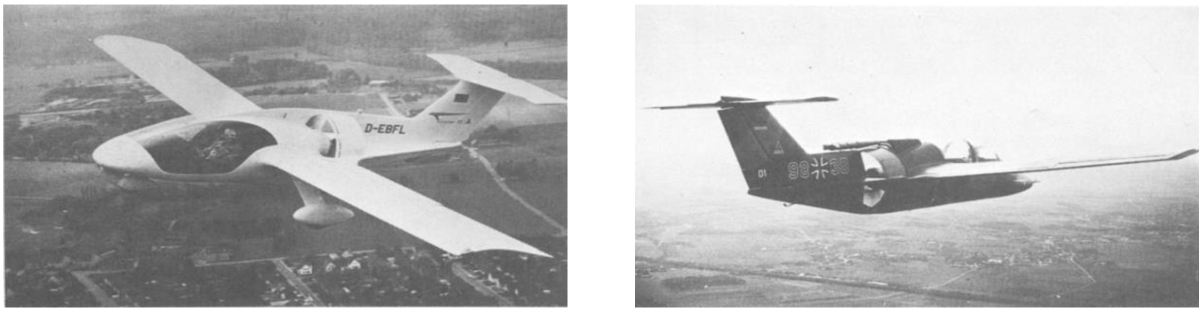

(a) Fanliner aircraft design (b) Fantrainer aircraft design

Figure 8: Channel wing aircraft by Rhein Flugzeugbau [34]

Meanwhile, AN-181 was an experimental channel wing aircraft built by Antonov in the 1980s [9] [35]. However, very little is known about its handling qualities. An Open Day sponsored by Antonov OKB attracted notice in 1990 when a research aircraft with the designation "181" made an unexpected appearance, which is depicted in Figure 9. The two channel wings on the aircraft were derived based on a design by W R Custer from the mid-1950s. According to Custer's design, a 180° half-barrel aerofoil profile provided powered lift [35]. In short, the '181' was powered by a 210 hp Czech M-337A piston engine, which turned the tractor propellers above the leading edge. Its unusual tail design was intended to maintain effectiveness at low airspeeds. The aircraft's claims were deemed to be implausible in spite of its attractive design and polish. In fact, the Antonov authorities acknowledged it possibly should not have been presented [35].

Figure 9: The AN-181 aircraft [35]

All in all, the historical timeline overview for the channel wing is tabulated in Table 1.

Table 1: Timeline of channel wing development

Year	Major Development
1921	French engineer Félix du Temple patents a "compound aircraft" design, which features a central channel between two wings. While not exactly the Channel-wing, it lays the groundwork for the concept.
1930's	Aircraft designers and engineers begin exploring unconventional wing designs to improve lift, stability, and efficiency.
1940's	Willard Ray Custer conceptualizes the channel wing idea, inspired by research into the effects of wind gusts on corrugated metal surfaces.
1950's	Custer develops the pusher system with a propeller placed at the trailing edge of the wing, forming the foundation for the channel wing concept.
1952	Patent and Innovative Configuration: Custer receives his first patent for a Channel-wing with jet propulsion. Describe the aircraft's design featuring a conventional fuselage, a channel-wing, and jet propulsion. Highlight the placement of the propellers close to the channel boundaries and the concept of variable pitch for improved flight performance.
1953	Empirical Testing and Evolution: Jerome Pasamanick conducts extensive tests on the Custer Channel Wing aircraft in full-scale tunnels. Describe the purpose of the tests and how they provided empirical evidence of the configuration's possibilities.
1970's	Rhein Flugzeugbau made great progress in less than ten years, producing popular aircraft as the Sirius 1, Sirius 2 gliders (1971), and the twin-seat light aircraft Fanliner (late 1973). This achievement inspired the development of the Fantrainer (1977) as researchers explored the evolution of the Rotary Engine in response to changing energy and material standards. Rhein Flugzeugbau increased the size and speed of its engines by utilizing the Rotary Engine's power density.
1980's	The '181' research aircraft's introduction in 1990 exhibited an unconventional design founded in Custer's mid-1950s concept, although it was met with skepticism due to its unrealistic claims. Antonov's experimental AN-181 channel wing aircraft from the 1980s also aroused issues.

In a recent paper published in 2020, the channel wing aircraft is mentioned as an illustration of a cutting-edge design that was a little ahead of its time. According to the report, the channel wing concept offers a classic illustration of an idea worth exploring with modern tools and technology to determine the degree to which its STOL performance might resemble VTOL [9].

4. Performance of Channel-Wing

Over the years, several research studies have been done to analyze aerodynamic wing performance of the channel-wing aircraft in various aspects, including the coefficient of lift, coefficient of drag, lift-to-drag ratio, and also takeoff and landing efficiency [36]-[39]. These investigations are aimed to identify parameters affecting the aerodynamic performance of the channel-wing aircraft to meet current aviation demands. However, as air transportation increased over the years, the demand for commercial aircraft also increased, leading to flight delay issues [40]-[42]. Furthermore, to accommodate more capacity for conventional aircraft in terminals, airports worldwide require longer runways, creating challenges for the civil aviation industry [41]-[44]. This limitation has led aviation experts to dream of introducing a highly efficient, multipurpose, small-size aircraft that qualifies for Short Takeoff and Landing (STOL) to address these issues [32]. The STOL capability is a challenge for current conventional aircraft as they must meet specific criteria such as the duration of a runway, land and water. The performance of the channel wing is significantly influenced by where the propellers and channel wing are mounted on the airplane. The aerodynamic installation effects of the over-the-wing propeller mounting arrangements, which enhance the performance of a channel-wing aircraft, have played a significant part in the study of channel-wing design [22]. This results in a higher lift coefficient of around 5 in comparison to the traditional airplane's lift coefficient of around 2. The Custer CCW-5 is the most efficient aircraft built by Willard Custer, and it can take off and land in a very small distance at a speed of 20 mph, or even vertically if the engines are powerful enough [8]. This aircraft's outstanding STOL qualities make it well-suited for transferring payloads in tough settings lacking extensive runways, making it extremely ideal for humanitarian missions across the world [9]. The lift coefficient increases as angle of attack increases, allowing the aircraft to ascend to greater heights while maintaining a high angle of attack of more than 20° without stalling. This unique feature makes it an excellent alternative for aircraft requiring a quick takeoff or rapid ascension to obtain altitude [31][36].

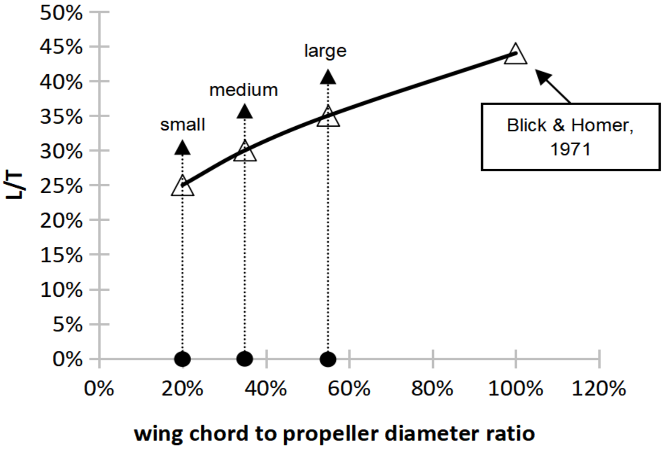

Figure 10: Relationship between lift-thrust performance and sizing of the channel-wing [22]

Previous research has explored the potential of channel-wing design to enable STOL capabilities [22], which would allow commercial or industrial complexes to have their own on-site aviation services while minimizing speed and range limitations. A study at Georgia Tech Research Institute (GTRI), the channel-wing has the potential to generate lift force even at a standstill and has a wider range of angle of attack before stalling (approximately -40° to +40°). The lift generated by the channel-wing could be twice that of a conventional wing and could even allow for zero ground roll take-off [8]. Furthermore, following another study at the University of Southampton on a small-unmanned fixed-wing aircraft to evaluate the superior slow-flight performance of the channel-wing design compared to a conventional wing-propeller configuration [45]. The study revealed that STOL capabilities could reduce cruise speed by up to 9%. Additionally, the coupling effects of a distributed multi-propeller channel wing at low-speed conditions have also been studied as illustrated in Figure 11 [10]. To integrate the propellers with the wing, the computational technique used RANS equations and the Momentum Source Method. The study's findings demonstrated that the airfoil shape has a considerable impact on the lift of the channel wing during the Short/Vertical Takeoff and Landing (S/VTOL) stage. Furthermore, the study of the multi-propeller channel wing revealed the critical function of rotational direction in the interaction of outer propellers, with outboard-up rotation increasing lift in the outer channel. Different distortion and dissipation behaviors were identified in the wake of the propellers, which were significantly impacted by the presence of nearby propellers. On the other hand, a study at Beijing University of Aeronautics and Astronautics investigated the use of a fuel-saving double channel-wing (FADCW) arrangement in a propeller-driven aircraft to reduce the fuel consumption, as shown in Figure 12 [46]. The study proved that the design improves the wing's aerodynamic performance by leveraging the suction effect upstream of the propeller and the slipstream acceleration downstream of the propeller. It achieved a stunning over 10% increase in lift-to-drag ratio and a significant more than 20% reduction in fuel consumption when compared to the typical TPC design by integrating the propeller. The findings further validate the feasibility of the proposed design idea, emphasizing its capacity to minimize the fuel consumption in propeller-driven aircraft, which has the potential to achieve more range or longer loiter time.

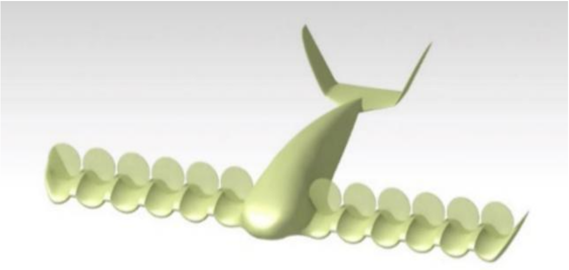

Figure 11: A model of the multi-propeller channel wing UAV [10]

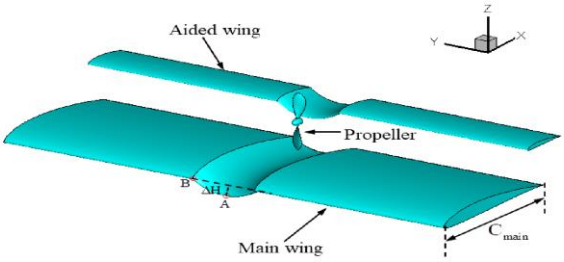

Figure 12: Fuel saving double channel wing configuration [46]

5. Available Patents of Channel-Wing Design

The filed patent of Taylor in 1954, displayed in Figures 13, was the first to feature a channel-wing design from someone other than Willard Custer. This patent combines the channel-wing idea with a movable mechanism that can alter the lift/thrust vectors and the aircraft's orientation. In short, the design consists of an aircraft with the semi-conventional fuselage situated and a channel on top and ailerons on either side. The propeller mount can be moved up, down, left, and right, allowing it to rotate in two dimensions. The aircraft primarily relies on the channel for lift, except for minor contributions from the fuselage's front area and the ailerons. To maintain stability, precise positioning of the aircraft's center of gravity is necessary. Meanwhile, Figures 14 shows the Fletcher's 1954 patent, which is a typical fuselage together with two wings that have four tilting channels placed at the ends of each wing. This patent successfully combines ideas from Custer and Taylor. A turboprop engine is housed within these channels. While hovering, climbing vertically or descending, the channels are modified to balance the lateral components of the lift and thrust vectors, producing an upward push. The channels tilt forward gradually as the airplane moves into forward flight and the aircraft's angle of attack is nearly zero. During these maneuvers, drag must also be considered.

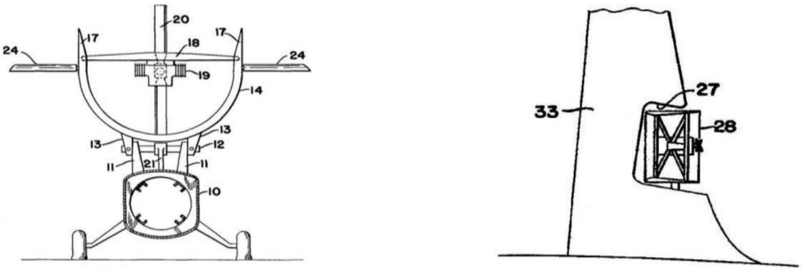

(a) Top mounted channel layout (b) Notched-channel design

Figure 13: Taylor’s channel wing aircraft design patent [11]

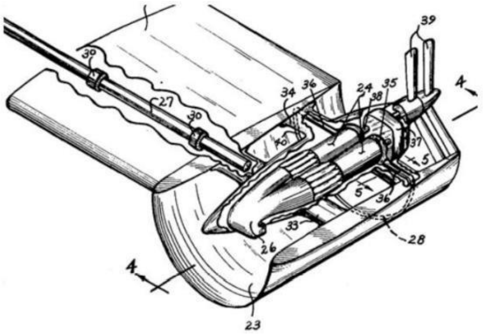

(a) BLR layout

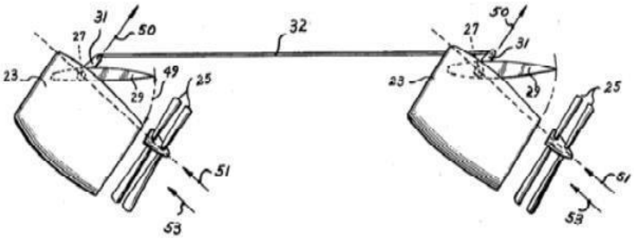

(b) Tilting channel configuration

Figure 14: Fletcher's channel wing aircraft design patent [11]

Moreover, Shew's invention as shown in Figure 15, was created in 1960. It includes two channels with a flying wing-like surface. The side plates that run through the entire length of the airplane and are fastened on both sides of the fuselage support the channels, which are located near to the front of the fuselage. The flaps and air brakes are two of the control surfaces included in this design. In addition, the bottom of the wing has additional vents that route the air in a way that promotes high lift. The high-speed airflow across the wing is controlled by these plates.

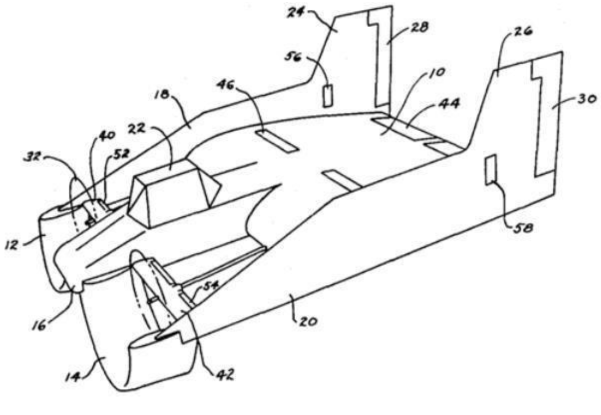

Figure 15: Shew's channel-wing layout [11]

In the meantime, the main goal of the current invention in Figure 16 is to create improved STOL aircraft that is able to land with or without power at relatively low speeds on unimproved, small airstrips while traveling at high speeds. This invention attempts to show that the wing arrangement in this design is suitable for a re-entry vehicle by folding the wings into an extended staggered stance and removing 90% of the drag. With less power, this idea also intends to increase speed variance from a very slow to a supersonic speed. Another objective of this construction is to make it as a vertical takeoff aircraft due to the design of its fuselage and wings. By using a double set of wings to create extremely large fuselage for increased load carrying capacity while maintaining the original design's gliding performance, this invention also aims to show that this wing layout is adaptable to a transport or cargo type aircraft [47].

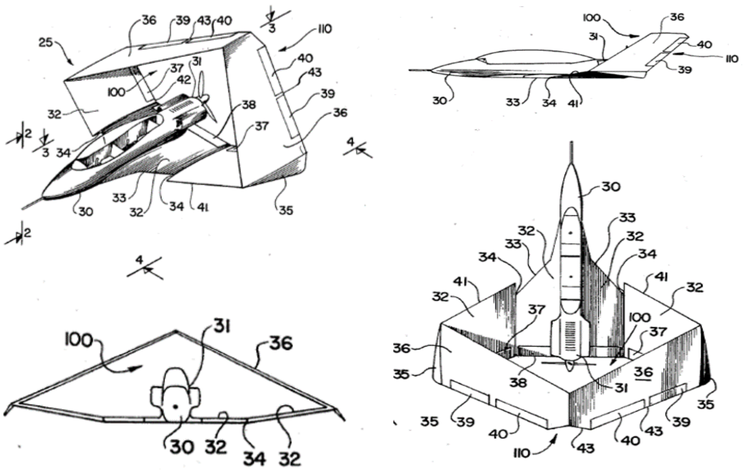

Figure 16: Patents on staggered channel wing-type aircraft [47]

Another current invention is illustrated in Figure 17, which is a pneumatic (blown) powered-lift aircraft is provided with significant increase in propulsive and aerodynamic forces. This permits flight control at these very low speeds, which is typically a considerable difficulty for Super STOL or VTOL aircraft, as well as the possibility for very low flight speeds and very short takeoff and landing distances. The significant improvement in flying safety is also the outcome of this better controllability and short response times. Furthermore, without using any moving parts, it is feasible to switch between thrust (needed for takeoff and ascent) and drag (needed for STOL approach). Because of its super STOL or VTOL characteristics, this aircraft can use short runways or landing pads. The propeller's position in this aircraft, located ahead of the channel's trailing edge and behind its leading edge, not only virtually eliminates ground-based noise perception but provides passengers with virtually complete protection against propeller contact. Unlike the typical Channel Wing aircraft with a sharp trailing edge, the blown channel CCW incorporates a channel characterized by rounded or nearly rounded trailing edge. This channel is equipped with a trailing-edge slot positioned adjacent to its rounded trailing edge. This slot is designed to allow the tangential discharge of the pressurized air over the rounded trailing edge and is connected to an intake linked to a source of pressurized air. The resultant jet effectively entrains the surrounding flow field and maintains the attachment to the rounded trailing edge, all thanks to the well-established Coanda effect [48].

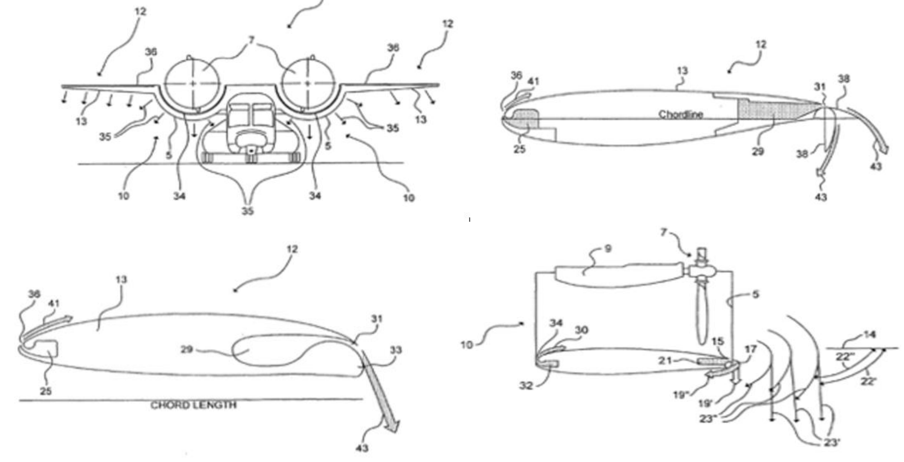

Figure 17: Channel wing system for thrust deflection and force/moment generation [48]

It is essential to note that the Aerodyne concept, as depicted in Figure 18, shows that the flow can deflect up to 26° at low airspeeds while just slightly deflecting at high airspeeds. This enables the channel wing to attain dependence on airspeed natural thrust vectoring capability. The propeller's location inside the wing channel and the fact that the effective exhaust blowing coefficient is larger at lower freestream velocities are the causes of this. A single channel has been used to successfully overcome the weaknesses relating to asymmetric lift during low-speed operations, an area where most channel wing flying tests ran into problems. It's important to note that Custer frequently used many channels while implementing the channel wing. Additionally, a single duct architecture adheres to the restrictions imposed by span limitations while offering the least amount of disc stress and the most ducted propeller area [49].

Figure 18: Lippisch Aerodyne concept in 1960s [49]

Figure 19 shows a patent that focuses on power that matches during takeoff and cruising between 125-150 mph on the same time maintaining the engine capacity not more than 100 hp. Leaning on the chances of blowing and trimming, this design of propulsion and aerodynamic combined make way of the possibility of utilizing maximum takeoff distance of 250 ft without supporting lift system actuating parts with maximum lift coefficient ranging from 6 up until 10. What prompted this ducted propeller idea was the effect it would make on propulsion system, which projected to cut down on its disc-loading and thus putting pressure on increasing the low-speed thrust, favorable for its safety appeals. A specific requirement on takeoff and landing field lengths, this patent should be able to manage the gust control reaching down to 30 mph on its rolling motion control during low-speed resulting to active blowing or oversizing the control surfaces. Though as promising as it might seem, this patents still have a lot of improvements that when implied to, may produce a better overall maneuverability. To move forward with the design, implementation of movable outer wing panel seems the most straightforward solution in managing the roll control of this aircraft and control surfaces in the propeller flow to cater its yaw and pitch control [49]-[50].

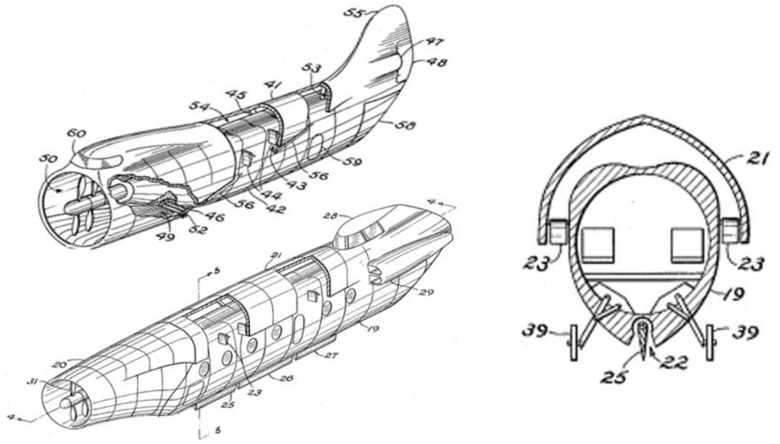

Figure 19 Patents on Aerodyne with External flow [50]

6. Conclusion

This paper provides an overview of the channel-wing design possibilities for STOL aircraft. This includes discussion of channel-wing design concept, a brief review of its early development, highlighting current research, assessing performance, patents, discussing limitations and bringing the prospect of the channel-wing for VTOL/STOL application. The concepts that surround the channel wing aircraft are the Coanda effect and U-shaped design of it, which were developed from avant-garde ideas in the middle of the 20th century, offering novel method of lift creation. Despite having difficulties compared to conventional aircraft designs, recent developments in pneumatic technology and modern equipment provide renewed promise. A convincing solution for STOL applications and potential solutions for the operational niches could result from reassessing its capabilities using contemporary methodologies. The channel-wing design has potential as aviation develops because of its distinct lift-enhancing principles and versatility in a range of flight scenarios. The development of channel wing demonstrates creative approaches to problems in aviation. Though there are several advantages, capabilities of the design do pose some challenges. This comprises an increase in drag owing to the profile shape and wetted surface area of the wing, as well as slight decrease in thrust due to pressure changes downstream of the propeller blade, which deflect the thrust force vector downward. Also, if one engine fails during flight, it causes an unbalanced lift force on the wing, making it more challenging to maintain stable flight. Despite that, it is still undeniable that its aerodynamic properties have been well-suited for the possibility of STOL applications. Its adaptability and efficiency improvements are also highlighted by notable studies like the multi-propeller channel wing and fuel-saving double channel wing configurations. With their ability to accommodate limited locations, humanitarian missions and better fuel efficiency, its developments' potential to reinvent aviation conventions has been positive once its design deficiencies are successfully addressed.

Acknowledgement

The authors want to thank and acknowledge Universiti Putra Malaysia on their continued support by way of the Industry Research Grant, Endowment Tan Sri Syed Azman (6338203-10801).

References

[1] D. Y. Suh and M. S. Ryerson, 'Forecast to Grow: Aviation Demand Forecasting in an Era of Demand Uncertainty and Optimism Bias', Transportation Research Part E: Logistics and Transportation Review, vol. 128, pp. 400-416, 2019.

[2] D. Hanson, T. T. Delibasi, M. Gatti and S. Cohen, 'How Do Changes in Economic Activity Affect Air Passenger Traffic? The Use of State-Dependent Income Elasticities to Improve Aviation Forecasts', Journal of Air Transport Management, vol. 98, 102147, 2022.

[3] A. Menichino, V. Di Vito, B. Dziugiel, A. Liberacki, H. Hesselink and M. Giannuzzi, 'Urban Air Mobility Perspectives Over Mid-Term Time Horizon: Main Enabling Technologies Readiness Review', Presented at the Integrated Communication, Navigation and Surveillance Conference, Dulles, USA, April 2022.

[4] A. Abdelghany and V. S. Guzhva, 'Exploratory Analysis of Air Travel Demand Stimulation in First-Time Served Markets', Journal of Air Transport Management, vol. 98, 102162, 2022.

[5] Y. Y. Tee and Z. W. Zhong, 'Modelling and Simulation Studies of the Runway Capacity of Changi Airport', The Aeronautical Journal, vol. 122, no. 1253, pp. 1022-1037, 2018.

[6] J. H. Diekmann, 'Flight Mechanical Challenges of STOL Aircraft using Active High Lift', Journal of Aircraft, vol. 56, no. 5, pp. 1753-1764, 2019.

[7] G. R. Seyfang, 'Recent Developments of the Fan-Wing Aircraft', Presented at the International Conference of the European Aerospace Societies, Venice, Italy, October 2011.

[8] R. Englar and B. Campbell, ‘Development of Pneumatic Channel Wing Powered-Lift Advanced SuperSTOL Aircraft’, Presented at AIAA Applied Aerodynamics Conference, St. Louis, USA, June 2002.
[9] D. M. Bushnell and I. Wygnanski, ‘Flow Control Applications’, Technical Report (L-21092), National Aeronautics and Space Administration, Washington DC, USA, 2020.
[10] J. Zhao, Z. Fan, M. Chang and G. Wang, ‘Coupling Effects on Distributed Multi-Propeller Channel Wing at Low Speed Condition’, Energies, vol. 15, no. 15, 5352, 2022.
[11] Z. O. Gokce and C. Camci, ‘Channel Wing as a Potential VTOL/STOL Aero-Vehicle Concept’, Recent Patents on Mechanical Engineering, vol. 3, no. 1, pp. 18-31, 2010.
[12] W. R Custer, Aircraft Channel Wing Propeller Combination, US Patent (US3123321A), 1964.
[13] H. R. Clements, ‘The Channel Wing Revisited’, Journal of Aerospace, vol. 115, pp. 550-562, 2006.
[14] C. Gunther, J. Marchman and R. VanBlarcom, ‘Comparison of Channel Wing Theoretical and Experimental Performance’, Presented at the Aerospace Sciences Meeting and Exhibit, Reno, USA, January 2000.
[15] R. J. Englar and B. A. Campbell, ‘Experimental Development and Evaluation of Pneumatic Powered-Lift Super-STOL Aircraft’, Presented at NASA/ONR Circulation Control Workshop, Hampton, USA, March 2004.
[16] D. M. Bushnell, Fluid Mechanics, Drag Reduction and Advanced Configuration Aeronautics, National Aeronautics and Space Administration, 2000.
[17] D. Bushnell, ‘Frontiers of the 'Responsible Imaginable' in (Civilian) Aeronautics’, Presented at the Aerospace Sciences Meeting and Exhibit, Reno, USA, January 1998.
[18] M. H. Sadraey, Aircraft Design: A Systems Engineering Approach, John Wiley & Sons, 2012.
[19] C. Y. Justin and D. N. Mavris, ‘Environment Impact on Feasibility of Sub-Urban Air Mobility using STOL Vehicles’, Presented at the AIAA Scitech Forum, San Diego, USA, January 2019.
[20] C. Courtin, M. J. Burton, A. Yu, P. Butler, P. D. Vascik and R. J. Hansman, ‘Feasibility Study of Short Takeoff and Landing Urban Air Mobility Vehicles using Geometric Programming’, Presented at the Aviation Technology, Integration and Operations Conference, Atlanta, USA, June 2018.
[21] W. Sellers, B. Singer and L. Leavitt, ‘Aerodynamics for Revolutionary Air Vehicles’, Presented at the AIAA Applied Aerodynamics Conference, Orlando, USA, June 2003.
[22] M. A. M. Shafie, M. F. Abdul Hamid and A. S. Mohd Rafie, ‘Circulation Control Aircraft Design: Assessment on the Channel-Wing Lift-Thrust Performance Characteristics’, Journal of Advanced Research in Fluid Mechanics and Thermal Sciences, vol. 64, no. 1, pp. 143-151, 2019.
[23] J. Sivapalan, A. S. Mohd Rafie, A. R. A. Talib, E. Gires, A. A. Basri, F. I. Romli, A. S. M. Harithuddin, S. A. Sobri and M. F. A. Hamid, ‘The Aerodynamic Lift Performance Analysis of Channel-Wing Design for STOL Aircraft’, Journal of Aeronautics Astronautics and Aviation, vol. 55, pp. 415-423, 2023.
[24] W. R. Custer, Aeroplane, US Patent (1,708), 1929.
[25] M. Zilberman, ‘Custer Channel Wing (CCW) Phase III’, Presented at the AIAA Scitech Forum, Online, January 2021.
[26] V. Stanciu and V. Dragan, ‘An Analytical and Numerical Study of the Custer Channel Wing Configuration’, International Journal of Advanced Scientific and Technical Research, vol. 4, pp. 1-8, 2012.
[27] J. Pasamanick, Langley Full-Scale-Tunnel Tests of the Custer Channel Wing Airplane, National Advisory Committee for Aeronautics, 1953.
[28] N. Intaratep, ‘The Investigation of an Inboard-Winglet Application to a Roadable Aircraft’, PhD Thesis, Virginia Tech, USA, 2002.
[29] R. Gimbert, A. Clos and S. Baty-Ferry, ‘Channel Wing Airplane’, Presented at TMAL02 Expert Conference, Linköping, Sweden, October 2017.

[30] R. H. Lange, 'Review of Unconventional Aircraft Design Concepts', Journal of Aircraft, vol. 25, no. 5, pp. 385-392, 1988.
[31] P. M. Keane and A. J. Keane, 'Use of Custer Channel Wings – Wing Ducts on Small UAVs', Journal of Aerospace Engineering, vol. 29, no. 3, 04015059, 2016.
[32] M. Chang, Z. Zheng, X. Meng, J. Bai and B. Wang, 'Aerodynamic Analysis of a Low-Speed Tandem-Channel Wing for eVTOL Aircraft Considering Propeller-Wing Interaction', Energies, vol. 15, no. 22, 2022.
[33] E. A. Willis, 'General Aviation Energy-Conservation Research Programs', Presented at Rotary Combustion Engine – Candidate for General Aviation Symposium, Cleveland, USA, February 1978.
[34] R. Staufenbiel, A. Kellner and G. Neuwerth, Dependence of Noise Generation by Rotors on Defined Disturbances in the Inflow, Springer-Verlag, 1979.
[35] E. Gordon and B. Gunston, Soviet X-Planes, Midland Pub, 2000.
[36] E. F. Blick and V. Homer, 'Power-on Channel Wing Aerodynamics', Journal of Aircraft, vol. 8, no. 4, pp. 234-238, 1971.
[37] L. Müller, D. Kozulovic, M. Hepperle and R. Radespiel, 'The Influence of the Propeller Position on the Aerodynamics of a Channel Wing', AIAA Journal, vol. 38, no. 5, pp. 784-792, 2012.
[38] M. Xiaoxuan, X. Ziyi, M. Chang and B. Junqiang, 'Performance Analysis and Flow Mechanism of Channel Wing Considering Propeller Slipstream', Chinese Journal of Aeronautics, vol. 36, no. 11, pp. 165-184, 2023.
[39] R. Nangia and M. Palmer, 'Channel and Arc Wing Aerodynamics with Propeller Effects for STOL Application', Presented at the 39th Aerospace Sciences Meeting and Exhibit, Reno, UA, January 2001.
[40] E. B. Peterson, K. Neels, N. Barczi and T. Graham, 'The Economic Cost of Airline Flight Delay', Journal of Transport Economics and Policy, vol. 47, no. 1, pp. 107-121, 2013.
[41] B. F. Santos, M. M. Wormer, T. A. Achola and R. Curran, 'Airline Delay Management Problem with Airport Capacity Constraints and Priority Decisions', Journal of Air Transport Management, vol. 63, pp. 34-44, 2017.
[42] S. S. Cavusoglu and R. Macário, 'Minimum Delay or Maximum Efficiency? Rising Productivity of Available Capacity at Airports: Review of Current Practice and Future Needs', Journal of Air Transport Management, vol. 90, 101947, 2021.
[43] J. F. O'Connell, 'The Global Airline Industry', in The Routledge Companion to Air Transport Management, Routledge, 2018.
[44] P. Belobaba, A. Odoni and C. Barnhart, The Global Airline Industry, John Wiley & Sons, 2015.
[45] J. Mihalik and A. J. Keane, 'Custer Channel Wings for Short Takeoff and Landing of Unmanned Aircraft', Journal of Aircraft, vol. 59, no. 1, pp. 196-205, 2022.
[46] H. Wang, W. Gan and D. Li, 'An Investigation of the Aerodynamic Performance for a Fuel Saving Double Channel Wing Configuration', Energies, vol. 12, no. 20, 3911, 2019.
[47] A. Ratony, Staggered Channel Wing-Type Aircraft, US Patent (US4053125A), 1976.
[48] R. Engler and D. Bushnell, Channel-Wing System for Thrust Deflection and Force/Moment Generation, US Patent (US20050029396A1), 2006.
[49] M. Moore, '21st Century Personal Air Vehicle Research', Presented at AIAA International Air and Space Symposium and Exposition: The Next 100 Years, Dayton, USA, July 2003.
[50] A. M. Lippisch, Aerodyne with External Flow, US Patent (US2918233A), 1959.

eISSN 3009-0520